Materials Today Bio 29 (2024) 101344

Contents lists available at ScienceDirect

Materials Today Bio

journal homepage: www.journals.elsevier.com/materials-today-bio

Nickel–titanium alloy porous scaffolds based on a dominant cellular structure manufactured by laser powder bed fusion have satisfactory osteogenic efficacy

Jiaming Lin [a,1], An Yan [b,1], Anfei Huang [a,1], Qinglian Tang [a], Jinchang Lu [a], Huaiyuan Xu [a], Yufeng Huang [a], Tianqi Luo [a], Zhihao Chen [a], Anyu Zeng [a], Xiaojun Zhu [a,*], Chao Yang [b,**], Jin Wang [a,***]

[a] Department of Musculoskeletal Oncology, State Key Laboratory of Oncology in South China, Guangdong Provincial Clinical Research Center for Cancer, Sun Yat-sen University Cancer Center, Guangzhou, 510060, China
[b] National Engineering Research Center of Near-net-shape Forming for Metallic Materials, Guangdong Provincial Key Laboratory for Processing and Forming of Advanced Metallic Materials, South China University of Technology, Guangzhou, 510640, China

ARTICLE INFO

Keywords:
Laser powder bed fusion (LPBF)
Nickel–titanium (NiTi) alloy
Cellular structure
Porous scaffold
Osteogenic efficacy

ABSTRACT

Nickel–titanium (NiTi) alloy is a widely utilized medical shape memory alloy (SMA) known for its excellent shape memory effect and superelasticity. Here, laser powder bed fusion (LPBF) technology was employed to fabricate a porous NiTi alloy scaffold featuring a topologically optimized dominant cellular structure that demonstrates favorable physical and superior biological properties. Utilizing a porous structure topology optimization method informed by the stress state of human bones, two types of cellular structures—compression and torsion—were designed, and porous scaffolds were produced via LPBF. The physical properties of the porous NiTi alloy scaffolds were evaluated to confirm their biocompatibility, while their osteogenic efficacy was investigated through both in vivo and in vitro experiments, with comparisons made against a traditional octahedral unit cell structure. NiTi alloy porous scaffolds can be nearly net-shaped via LPBF and exhibit favorable physical properties, including a low elastic modulus, high hydrophilicity, a specific linear expansion rate, as well as superelastic and shape memory effects. These scaffolds demonstrate excellent biocompatibility, support in vitro osteogenesis, and possess significant in vivo bone ingrowth capabilities. When compared to titanium alloys, NiTi alloys show comparable osteogenic properties in vitro but superior bone ingrowth properties in vivo. Additionally, among octahedral-type, torsion-type, and topologically optimized compression-type porous scaffolds, the latter demonstrates enhanced bone ingrowth properties. LPBF technology is effective for manufacturing porous NiTi alloy scaffolds with fine pore structures and excellent mechanical properties. The scaffolds based on topologically optimized dominant cellular structures facilitate satisfactory and efficient bone formation.

1. Introduction

Confronted with bone defects caused by various diseases, 3D printing technology enables the personalized customization of bone repair implants. 3D-printed metal scaffolds, including titanium alloys, tantalum alloys, and degradable alloys, have been widely adopted in the field of bone repair. Due to their corrosion resistance, excellent biocompatibility, and enhanced strength-to-weight ratio, titanium and its alloys can be effectively utilized to fabricate customized implants that conform to an individual's anatomical structure, making them suitable for various

* Corresponding author. Department of Musculoskeletal Oncology, Sun Yat-sen University Cancer Center, 651 Dongfeng East Road, Guangzhou, Guangdong, 510060, China.
** Corresponding author. National Engineering Research Center of Near-net-shape Forming for Metallic Materials, South China University of Technology, Guangzhou, 510640, China.
*** Corresponding author. Department of Musculoskeletal Oncology, Sun Yat-sen University Cancer Center, 651 Dongfeng East Road, Guangzhou, Guangdong, 510060, China.
E-mail addresses: zhuxj@sysucc.org.cn (X. Zhu), cyang@scut.edu.cn (C. Yang), wangjinbs@sysucc.org.cn (J. Wang).
[1] Jiaming Lin, An Yan and Anfei Huang have contributed equally to this study and therefore share first authorship.

https://doi.org/10.1016/j.mtbio.2024.101344
Received 2 August 2024; Received in revised form 30 October 2024; Accepted 14 November 2024
Available online 15 November 2024

types of bone repair prostheses [1]. Porous tantalum scaffolds are noted for their high biocompatibility and low friction coefficient. Their 3D-printed biomimetic porous structure and mechanical properties closely resemble those of human bone tissue, making them a significant focus of research in bone defect repair [2]. The application of 3D printing technology also holds the potential to produce biodegradable implants with a porous structure, which can mitigate the stress shielding effects commonly associated with traditional implants and eliminate the need for secondary surgeries to remove them [3]. However, these alloy implants lack superelastic and deformable shape memory effects, and they may not accurately address complex, irregular bone defects, potentially resulting in excessive porosity or angulation. Additively manufactured deformable prostheses are urgently needed in the field of bone defect repair. Additively manufactured Nickel-titanium (NiTi) alloy prostheses theoretically possess a deformable effect that may fulfill this clinical requirement. NiTi alloy is a widely utilized medical shape memory alloy (SMA). Due to its favorable shape memory effect and superelasticity, it finds extensive application in orthopedic implants, including arched connectors [4–8], artificial ribs [9], arc nails [10], patellar concentrators [11], three-dimensional memory alloy fixation systems [12], spinal rods [13], and interbody fusion devices [14,15]. However, most clinically used NiTi implants are solid components produced through traditional processing technologies, which restrict their application in bone defect repair.

The design of a porous structure creates essential conditions for the growth of new bone within the repair prosthesis, thereby facilitating fusion between the prosthesis and the bone interface [16]. Porous scaffolds with varying unit cell structures exhibit distinct physical properties and osteogenic characteristics [17,18]. The dominant cellular structure is characterized by favorable physical properties, such as a low elastic modulus and high strength, as well as superior biological properties, including cell compatibility, osteointegration, osteoconductivity, and osteoinductive activity. Consequently, scaffolds based on the dominant cellular structure possess greater potential for precise repair in the domain of bone defect restoration.

Porous NiTi alloy structures produced through conventional manufacturing processes [19–24] have demonstrated good biocompatibility and osteogenic performance both in vitro and in vivo. Solid NiTi alloy structures created using laser powder bed fusion (LPBF) technology exhibit favorable biocompatibility in vivo [25]. Furthermore, the porous structure of NiTi alloys fabricated via LPBF possesses high strength and a low elastic modulus that fulfill the requirements for orthopedic implants [22,26], along with good biocompatibility [27] and excellent in vitro osteogenic performance [28,29].

The bones in various regions of the human body exhibit unique trabecular distribution and structural characteristics due to the differing stresses they experience. Consequently, bionic bone repair scaffolds must replicate these features. To address this need, topology optimization has emerged as a viable design strategy. This approach aims to redistribute material within the design space to achieve either minimum flexibility or maximum stiffness while adhering to specific stress and strain constraints [30–32]. Furthermore, porous structures have been developed that can not only withstand physiological loads but also be tailored to specific anatomical bone regions, thereby enhancing the functionality and compatibility of biomedical implants. However, reports on topologically optimized porous NiTi alloy structures remain scarce. Thus, there is an urgent clinical demand for the production of porous NiTi alloy scaffolds featuring topologically optimized dominant cellular structures through additive manufacturing technology. The impact of these topologically optimized dominant cellular structures, based on the actual stress state, on osteogenic efficiency remains uncertain.

In this study, a method for optimizing the topology of porous structures based on the stress state of human bones was employed to enhance the unit cell structures. A variable density approach utilizing a penalty topology optimization mathematical model was implemented. Focusing on the stress characteristics of load-bearing bones, such as the femur and vertebrae, the maximization of stiffness was established as the design objective, with the volume fraction serving as the constraint. Two types of porous cellular structures were designed: compression and torsion. Following model reconstruction, the porous implant scaffold model was produced and manufactured using additive manufacturing technology, specifically LPBF. Both in vitro and in vivo experiments demonstrated that the LPBF NiTi alloy porous scaffold, which is based on the predominant compression-type cellular structure, exhibits superior osteogenic efficacy compared to the traditional octahedral unit cell structure. This study offers a significant reference point for the clinical personalization of customized prostheses that feature topologically optimized dominant cellular structures based on actual stress conditions.

2. Materials and methods

2.1. LPBF formation process for NiTi alloy porous scaffolds

The received Ni50.4Ti49.6 (chemical composition: %) (Beijing AMC Powder Co., Ltd., China) was prepared using electrode induction melting gas atomization technology. The technical parameters of the LPBF process were as follows: the laser scan path alternated between adjacent layers by ±45° relative to the x-axis. In this study, the laser power, scanning speed, layer thickness, and hatch spacing were set to 80 W, 500 mm/s, 30 μm, and 80 μm, respectively.

The dimensions of the porous scaffolds for in vitro biological experiments were 10 × 10 × 2 mm, while the cylindrical porous scaffolds for in vivo animal experiments measured φ3 × 5 mm. Additionally, the cubic porous scaffolds for related physical property tests were sized at 10 × 10 × 10 mm. Employing a variable density method with a penalty topology optimization mathematical model, which is based on the force distribution of human load-bearing bones (such as femurs and vertebrae), the design aimed for stiffness maximization under volume fraction constraints. Two types of porous cellular structures were designed: compression and torsion. Following model reconstruction, the porous implant scaffold model was output and manufactured using additive manufacturing (LPBF). The porous NiTi alloy scaffolds were fabricated using an EOS M280 machine (EOS GmbH, Germany) in a high-purity argon atmosphere.

The porous scaffold underwent ultrasonic cleaning in ethanol and double-distilled water for 15 min, was dried in a furnace at 65 °C for 1 h, sterilized in an autoclave at 120 °C for 30 min, and was subsequently prepared for in vitro and in vivo studies.

2.2. Physical property characterization of the porous NiTi alloy scaffolds

2.2.1. Scanning electron microscopy observation

To investigate the surface morphology and microstructure of the porous alloy scaffolds, a scanning electron microscope (Philips XL-30 FEG) was employed to assess the morphology and compositional characteristics of different scaffolds (n = 3).

2.2.2. Water contact angle measurement

The water contact angles of the three groups of porous NiTi alloy scaffolds were measured using a contact angle meter (KRUSS, DSA25, Hamburg, Germany). Water droplets of equal volume were dropped vertically onto the surfaces of the various porous scaffolds, and the shapes of the contact droplets were captured using a compatible camera. The water contact angles were subsequently analyzed, and the average values were recorded and calculated (n = 3).

2.2.3. Compression test and functional characteristic test

The phase structure and composition were characterized using X-ray diffraction (XRD, PANalytical X'Pert Powder) with Cu Kα radiation, operating at 40 kV and 30 mA. Scanning was performed over a range of

30°–100° at a rate of 12°/min. Additionally, a NETZSCH 204 F1 differential scanning calorimeter (DSC) was utilized to assess the phase transformation temperatures of the 3 x 2 × 2 mm pony-size porous NiTi scaffold. Measurements were conducted within a temperature range of −40 to 75 °C, with heating and cooling rates of 10 °C/min in a nitrogen atmosphere, in accordance with ASTM F2004-05 standards. The DSC results indicate that the NiTi porous scaffolds exhibit both superelasticity and the shape memory effect at room temperature. Consequently, a compressive fracture test was conducted with increasing strains of 4 % and 6 % during thermodynamic cycling. For the thermodynamic cycle tests, samples were first immersed in ice water for 30 s before each test. Following the application of pre-strain, samples were unloaded and then immersed in hot water at 45 °C for 30 s to measure their recovered length. The loading and unloading processes, with a fixed strain rate of 1.8 x 10^{-4} s^{-1}, were monitored using an epsilon low-temperature extensometer (3442-010M-050M-LHT) attached to the compression grips, while the environmental chamber temperature was maintained at 26 °C. The elastic modulus was calculated based on the slope of the elastic segment of the compressive stress-strain curve (n = 3).

2.2.4. Porosity and pore size testing

Micro-computed tomography (Micro-CT) analysis of the porosity and pore size of porous NiTi alloy and porous Ti alloy scaffolds was conducted using a Diondo d2 scanner (Diondo GmbH, Germany) with a sample size of n = 5. Prior to initiating each experiment, a series of flat-field and dark-field images were captured with the beam turned off to minimize noise. All porous NiTi alloy scaffolds were rotated 360°, and two-dimensional (2D) projection images were collected at each angle, which were subsequently reconstructed and analyzed using VGStudio MAX 2.26 (Volume Graphics GmbH, Heidelberg, Germany). The reconstructed three-dimensional (3D) micro-CT model was compared with the designed Computer-Aided Design (CAD) model to determine the pore size deviation of the porous NiTi alloy scaffold.

2.2.5. Ion release experiment

The porous scaffolds were placed in a centrifuge tube and immersed in phosphate-buffered saline (PBS) at a scaffold surface area to extraction medium volume ratio of 1 cm^2/mL. To quantify the nickel ions released from the device over time, all of the extractant was removed at specified intervals, and a new solution was injected to continue the extraction process. This procedure was repeated until the extraction for all predetermined time points was completed. Nickel (Ni^{2+}) and titanium (Ti^{4+}) concentrations were measured on the 1st, 3rd, 5th, 7th, 14th, 21st, and 28th days of immersion. The samples were immediately analyzed using the same inductively coupled plasma spectrometer (ICP-OES, Agilent 720 ES, Australia) with n = 3 replicates.

2.3. Protein adsorption assay

The porous alloy scaffolds were placed in a 24-well plate, with three scaffolds per group. Five hundred microliters of a 1 g/L bovine serum albumin (BSA) solution was added to each well. After incubation at 37 °C for 1 h, the various porous scaffolds were gently washed three times with PBS. The proteins adsorbed onto the scaffolds were subsequently eluted with 500 μl of a 2 % sodium dodecyl sulfate (SDS) solution to obtain test samples. The protein concentration was determined using a bicinchoninic acid (BCA) protein concentration determination kit (Beyotime, China). The same method was employed to assess the protein content adsorbed onto the porous titanium alloy scaffolds after a 24-h incubation at 37 °C (n = 3).

2.4. Isolation, culture and identification of rat bone marrow mesenchymal stem cells

Sprague-Dawley (SD) rats were obtained from the Guangdong Medical Laboratory Animal Center. All procedures adhered to the guidelines set forth by the Animal Ethics Committee of the Sun Yat-sen University Cancer Center (Approval number: L025501202108003). Rat bone marrow mesenchymal stem cells (rBMSCs) were isolated from the bone marrow of two-week-old rats, as previously described [33]. Specifically, the femurs and tibiae were aseptically dissected following euthanasia of the rats. The bone marrow was extracted from the diaphysis by flushing with minimal essential medium alpha basic (α-MEM, Gibco, USA), collected by centrifugation, and cultured in a humidified atmosphere consisting of α-MEM, 10 % (v/v) fetal bovine serum (FBS, Gibco, USA), and antibiotics (100 units/mL penicillin and 100 μg/mL streptomycin; Gibco, USA) at 37 °C with 5 % CO2. The culture medium was replaced every three days. When the adherent cells reached approximately 80 % confluence, the rBMSCs were passaged using 0.25 % trypsin (Gibco, USA). Following purification and three passages, the cells were characterized by flow cytometry (Fig. S1) and utilized for subsequent experiments.

2.5. In vitro cytotoxicity assay

In accordance with the methods outlined by the International Organization for Standardization (ISO) 10993-5, the biosafety of the porous alloy scaffolds was assessed through in vitro cytotoxicity tests. The titanium alloy scaffolds, which were cleaned and disinfected, were immersed in cell culture medium at a scaffold surface area to extraction medium volume ratio of 1 cm^2/mL. The scaffolds were then incubated at a constant temperature of 37 °C for 72 h, after which the medium was collected for use in the experimental group. The negative control group was regular cell culture medium (noncytotoxic), while the positive control group contained cell culture medium supplemented with 10 % dimethyl sulfoxide (DMSO; Aladdin Biochemical Technology Co., Ltd., China) (cytotoxic).

rBMSCs in the logarithmic growth phase were digested using 0.25 % trypsin and centrifuged; the supernatant was discarded, and the cells were resuspended in cell culture medium to create a single-cell suspension. The cell density was adjusted to 1 × 10^5 cells/mL, and 100 μL of the cell suspension was added to each well of a 96-well plate, followed by incubation in a constant temperature incubator with 5 % CO_2 at 37 °C for 24 h. Once the cells adhered to the wells, the original cell culture medium was aspirated and replaced with either the negative control group medium, the experimental medium, or the positive control group medium, after which the cells were cultured at 37 °C. Three replicates were established for each group in the 96-well plates. On the 1st, 3rd, and 7th days of culture, one of the 96-well plates was removed, and 10 μL of Cell Counting Kit-8 solution (CCK-8, MedChemExpress, USA) was added to each well under light-proof conditions, followed by incubation at 37 °C for 2 h. The optical density (OD) at a wavelength of 450 nm was measured using a multifunctional microplate reader, and the relative cell proliferation rate was subsequently calculated.

2.6. Scanning electron microscopy observation of cell morphology

Following cleaning and disinfection, various porous scaffolds were placed in 24-well plates. The digested and resuspended rBMSCs were then inoculated directly onto each porous titanium alloy scaffold at a density of 5 × 10^4 cells per well and cultured in a constant temperature incubator at 37 °C for 7 days. The samples were washed carefully four times with sterile PBS, fixed in 2.5 % glutaraldehyde at room temperature for 2 h, and subsequently washed three times with sterile PBS. Gradient ethanol was employed for dehydration, with samples subjected to 10-min treatments in 50 %, 70 %, 80 %, 90 %, 95 %, and 100 % ethanol. After drying, the samples were coated with a gold film, and the cell morphology on the surface of the porous titanium alloy scaffold was observed using a scanning electron microscope (Philips XL-30 FEG).

2.7. Live/dead cell staining

rBMSCs were directly inoculated onto the porous scaffolds following the methods outlined in section 2.6. The cells were cultured in a constant temperature incubator at 37 °C with 5 % CO2 for either 3 days or 7 days, after which live/dead cell staining was conducted. Each porous scaffold, post-cleaning and disinfection, was immersed in cell culture medium, maintaining a surface area to volume ratio of 3 cm^2/ml. The scaffolds were incubated in a constant temperature incubator at 37 °C for 72 h, resulting in 100 % of the extract being utilized to culture the rBMSCs in the experimental group. The negative control group consisted of regular cell culture medium (non-cytotoxic), while the positive control group comprised cell culture medium containing 10 % DMSO (cytotoxic). The cells were cultured for 3 days or 7 days, followed by live/dead cell staining.

2.8. Laser confocal microscopy observation

After coculturing rBMSCs on each porous scaffold for 7 days, the samples were removed and gently rinsed with PBS three times, with each rinse lasting 10 min. Each sample was then fixed with 4 % paraformaldehyde at room temperature for 30 min and subsequently washed with PBS three times, each for 10 min. Following this, 0.1 % Triton X-100 (Thermo Fisher Scientific, USA) was applied for 10 min, after which the samples were washed again with PBS three times, each rinse lasting 10 min. Next, 200 μl of 100 nM phalloidin (UElandy, China) was added and incubated at room temperature in the dark for 1 h, followed by washing with PBS three times, each for 10 min. Subsequently, 200 μl of 5 μg/ml 4′,6-Diamidino-2′-phenylindole (DAPI) (Beyotime, China) was added to stain the nuclei for 5 min, and the samples were washed with PBS three times, each for 10 min. Finally, the morphological structure of the cells was observed using a laser confocal microscope (LSM 980, ZEISS, Germany).

2.9. Alkaline phosphatase activity detection and quantitative analysis

rBMSCs were cultured in media containing extracts from four types of porous scaffolds, and alkaline phosphatase (ALP) staining was conducted after 7 and 14 days of osteogenic induction. The control group was maintained in regular basal cell medium. Following the 7 and 14 days of culturing rBMSCs in osteogenic induction medium, the culture medium was discarded, and the samples were washed three times with PBS, each wash lasting 5 min. Subsequently, 4 % paraformaldehyde was applied to fix the samples for 30 min at 4 °C, after which they were again washed three times with PBS for 5 min each. Next, a working solution of 5-Bromo-4-chloro-3-indolyl phosphate/Nitrotetrazolium Blue chloride (BCIP/NBT) (Beyotime, China) was added to each well in accordance with the manufacturer's instructions, ensuring that the samples were completely covered. The samples were then incubated in the dark at room temperature for 30 min. After incubation, the staining solution was discarded, and the samples were washed three times with distilled water to halt color development, followed by observation and photography of the samples.For the quantitative analysis, the same method was employed. At each time point, the cells on the surface of the titanium alloy scaffold were lysed using cell lysis buffer, and the protein concentration was quantified using a BCA protein concentration assay kit (Beyotime, China). Subsequently, alkaline phosphatase activity was assessed using an alkaline phosphatase colorimetric assay kit (Beyotime, China) and was quantified relative to the protein concentration.

2.10. Alizarin red staining and quantitative analysis

The group settings and processing were consistent with those described in section 2.9. After culturing the rBMSCs for 14 and 21 days, the culture medium was discarded, and the cells were washed three times with PBS, each wash lasting 5 min. Subsequently, 4 % paraformaldehyde was added for fixation at 4 °C for 30 min, followed by two rinses with double distilled water, each lasting 5 min. One milliliter of Alizarin Red S (ARS) dye solution (40 mM) (Leagene, China) was added to each well and incubated at room temperature for 20 min. The cells were then rinsed with double distilled water while oscillating to remove any unbound dye, with the rinsing process repeated four times, each lasting 5 min. After gently rocking the cells for 5 min, the remaining double distilled water was aspirated, and the cells were observed and photographed. The calcium nodule precipitates on the samples were eluted using a 10 % cetylpyridinium chloride aqueous solution for 10 min at 37 °C, and the absorbance of the solution at 540 nm was recorded using a microplate reader.

2.11. RT−PCR detection of osteogenesis-related gene expression

After culturing rBMSCs on four types of porous scaffolds for 7 and 14 days in osteogenic induction medium, total ribonucleic acid (RNA) was extracted using TRIzol. The control group was maintained in regular basal cell medium. Relative RNA expression levels were assessed via quantitative real-time polymerase chain reaction (qRT−PCR), utilizing the housekeeping gene glyceraldehyde-3-phosphate dehydrogenase (GAPDH) as the loading control. All PCR amplifications were conducted in a final reaction volume of 20.0 μL, with the relative primer sequences provided in Table S1. The amplification reaction was executed using Hieff® qPCR SYBR® Green Master Mix (Yeason, 11201ES03, China) for 40 cycles, and relative expression levels were calculated according to the $2^{-\Delta\Delta Ct}$ method.

2.12. Osteogenesis-related protein expression

The group settings and processing were consistent with those described in section 2.11. Following culture for 7 and 14 days, total protein was extracted from the rBMSCs using radioimmunoprecipitation assay (RIPA) lysis buffer, and the protein concentration was quantified using the BCA assay. Equal amounts of protein were separated by sodium dodecyl sulfate−polyacrylamide gel electrophoresis (SDS−PAGE) and subsequently transferred onto a pure nitrocellulose blotting membrane. The membranes were blocked with 5 % (w/v) skim milk at room temperature for 1 h, and then incubated overnight at 4 °C with primary antibodies against osteopontin (OPN) (1:1000 dilution, AF0227, affinity) and Runt-related transcription factor 2 (RUNX-2) (1:1000 dilution, AF5186, affinity). After washing, the membranes were incubated with appropriate peroxidase-conjugated secondary antibodies (anti-rabbit and anti-mouse), and the immune complexes were detected using the ProLight horseradish peroxidase (HRP) Kit.

2.13. In vivo osteogenesis assay

2.13.1. Repair of distal femoral bone defects with porous scaffolds

In accordance with international standards, the in vivo animal experiments were approved by the Animal Ethics Committee of the Sun Yat-sen University Cancer Center (Approval number: L025501202108003). Twenty-four 10-week-old SD rats, each weighing between 350 and 400 g, were purchased from the Guangdong Medical Laboratory Animal Center. The experimental animals were housed in polypropylene cages maintained at a temperature of 20–25 °C and a humidity of 50–55 %, and they were fed a standard diet. All rats were randomly divided into two time points (4 weeks and 12 weeks), with each time point further divided into four groups, containing three rats per group, resulting in a total of 24 rats.

The bone defect model of the distal lateral condyle of the femur was selected for this study. General anesthesia was induced through isopentane inhalation. Following local skin preparation and disinfection, incisions were made layer by layer through the skin, subcutaneous fat, and muscle until the lateral condyle of the distal femur was exposed. A 3 mm diameter drill was used to create the bone defect, which was then

rinsed with saline. A cylindrical porous scaffold was inserted into the drilled hole (bone defect) between the condyles, positioned perpendicularly to the longitudinal axis of the left femur's distal lateral condyle (Fig. 8A).

The incision was subsequently sutured layer by layer: the muscle was closed with 6–0 absorbable sutures, while the skin was closed with 4–0 nonabsorbable sutures. At 4 weeks and 12 weeks post-implantation, the SD rats were euthanized via carbon dioxide inhalation, and the specimens containing the scaffolds were excised and fixed in 4 % paraformaldehyde for 24 h for further analysis.

2.13.2. Micro-CT scanning

To evaluate the bone ingrowth properties of porous scaffolds implanted into rat bone defects, harvested scaffold samples were subjected to micro-CT analysis using a Diondo d2 scanner (Diondo GmbH, Germany). The scanning parameters included an accelerating voltage of 110 kV, a current of 110 mA, an X-ray tube focus-to-object distance of 802 mm, an X-ray tube focus-to-flat-panel detector distance of 64 mm, a voxel size of 4 μm, and a resolution of 0.008. Prior to each experiment, a set of flat-field and dark-field images was captured with the beam turned off to eliminate noise. All porous NiTi alloy scaffolds were rotated 360° to ensure complete irradiation within the detection range. Two-dimensional (2D) projection images were collected at each angle and subsequently reconstructed and analyzed using VGStudio MAX 2.26 (Volume Graphics GmbH, Heidelberg, Germany). The scaffolds and the bone tissue growing in and around the internal space of the scaffold were defined as volumes of interest for detailed data analysis. The bone volume divided by total volume (BV/TV%), trabecular number (Tb.n), and trabecular thickness (Tb.Th) were calculated to quantitatively assess bone ingrowth performance.

2.13.3. Histological evaluation

After fixation for one day, the samples collected were dehydrated using a graded ethanol series. Subsequently, the samples were embedded in a methyl methacrylate solution at 37 °C for one week. The polymer blocks were then sectioned into thin slices, approximately 100 μm thick, perpendicular to the long axis of the scaffold using an interlocking diamond saw (Leica Microtome, Germany). To assess bone growth within the porous scaffolds, the sections were stained with methylene blue-acid magenta stain and Goldner's trichrome stain.

2.14. Statistical analysis

All experimental results in this study were obtained from at least three independent samples or from more than three independent experiments. The data are presented as means ± standard deviations (SDs). Data analysis was conducted using IBM SPSS Statistics 20 software. One-way ANOVA was employed for comparisons between datasets, while Tukey's analysis was utilized for multiple comparisons between groups. Statistical significance was defined as $^{*}P < 0.05$, $^{**}P < 0.01$, $^{***}P < 0.001$, and $^{****}P < 0.0001$ for all statistical tests. All statistical graphs were generated using GraphPad Prism 9.5 software.

3. Results and discussion

3.1. Design of the NiTi alloy porous scaffold and LPBF molding

This study focuses on various load-bearing skeletal components of the human body. The cellular structure of a porous structure was designed and optimized in accordance with the internal unit stress state present in the service environment. Initially, a model of the human skeletal system was constructed using computed tomography (CT) scan data. A biomechanical simulation was conducted to extract the three-dimensional stress state of a representative unit of the corresponding skeletal parts, leading to the optimization of the pore structure topology. Following model reconstruction, the porous implant model was produced using additive manufacturing techniques. Furthermore, the pore size of the designed porous structure was adjusted to satisfy the requirements for different contact orientations, including biological tissue cell adhesion, proliferation, and differentiation. This adjustment aims to achieve precise control over the biological behavior of tissue cells with varying pore parameters, thereby ensuring the production of high-quality porous prostheses.

A porous structure topology optimization method, based on the stress state of human bones, was employed to design two distinct types of porous cellular structures: compression and torsion types. Fig. 1B and C illustrate the process of porous structure topology optimization. Fig. 1D–F presents three types of cellular structures: the traditional octahedral type (D), the topologically optimized compression type (E), and the torsion type (F), accompanied by schematic diagrams of the corresponding porous scaffolds.

Three types of porous scaffolds with varying cellular structures were manufactured using LPBF technology. The flowchart depicting the fabrication process of the scaffolds is presented in Fig. 1A. As illustrated in Fig. 1G, LPBF-processed NiTi alloy porous scaffolds, featuring compression, octahedral, and torsion cell structures, were compared to a titanium alloy (Ti-6Al-4V) porous scaffold with an octahedral cell structure, which served as the control group. The dimensions of the porous scaffold utilized for in vitro biological experiments were 10 mm × 10 mm × 2 mm. For in vivo animal experiments, the cylindrical porous scaffold measured φ3 mm × 5 mm, while the cubic porous scaffold employed for physical performance tests was 10 mm × 10 mm × 10 mm in size.

The porous scaffolds were examined using scanning electron microscopy (SEM). The imaging results indicated that the LPBF-formed porous scaffolds closely matched the designed model in both appearance and internal cellular structure. Fig. 1H–K displays a compression-type NiTi alloy porous scaffold (NiTi-C), an octahedral-type NiTi alloy porous scaffold (NiTi-O), a torsion-type NiTi alloy porous scaffold (NiTi-T), and an octahedral-type titanium alloy porous scaffold (TC4-O), respectively.

3.2. Physical properties of the porous NiTi alloy scaffolds

Fig. 2A illustrates that the water contact angle of the NiTi-C porous scaffold is a small acute angle, averaging approximately 24°. In contrast, the water contact angles of the NiTi-O and NiTi-T porous scaffolds are significantly larger, averaging approximately 118° and 114°, respectively, as shown in Fig. 2B and C. Notably, the water contact angle of the NiTi-C is less than 90°. These results are superior to those reported by Hoffmann et al. [28], indicating that NiTi alloy scaffolds possess enhanced hydrophilic properties [34].

The porosities and pore sizes of the four porous scaffolds were measured using micro-CT. Previous studies have demonstrated that porosity and pore size significantly influence bone formation, with a porosity exceeding 40 % [35,36] and a pore size greater than 300 μm [37] generally deemed sufficient to support vascularization and bone ingrowth [38,39]. In this study, Fig. 2D illustrates the structural porosities [40] of the porous scaffolds. The results indicate that the structural porosities of NiTi-C, NiTi-O, NiTi-T, and TC4-O are 47.77 %, 47.34 %, 47.89 %, and 47.92 %, respectively. These structural porosities are nearly 50 %, representing approximately a 20 % deviation from the design value of 70 %. This deviation primarily arises from the intrinsic phenomenon whereby the laser melt pool is larger than the laser beam spot [41]. Fig. 2E presents the strut sizes and pore sizes of the different porous scaffolds. Notably, NiTi-C exhibits the largest pore size at 568.4 μm, followed by NiTi-T with a pore size of 476 μm, while NiTi-O has the smallest pore size at 410 μm. The water contact angle is influenced by the type of unit cell structure; thus, the larger pore size of NiTi-C contributes to its enhanced permeability compared to the other two cellular structures. These findings align with the results regarding the water contact angle, indicating that when pore size reaches a certain

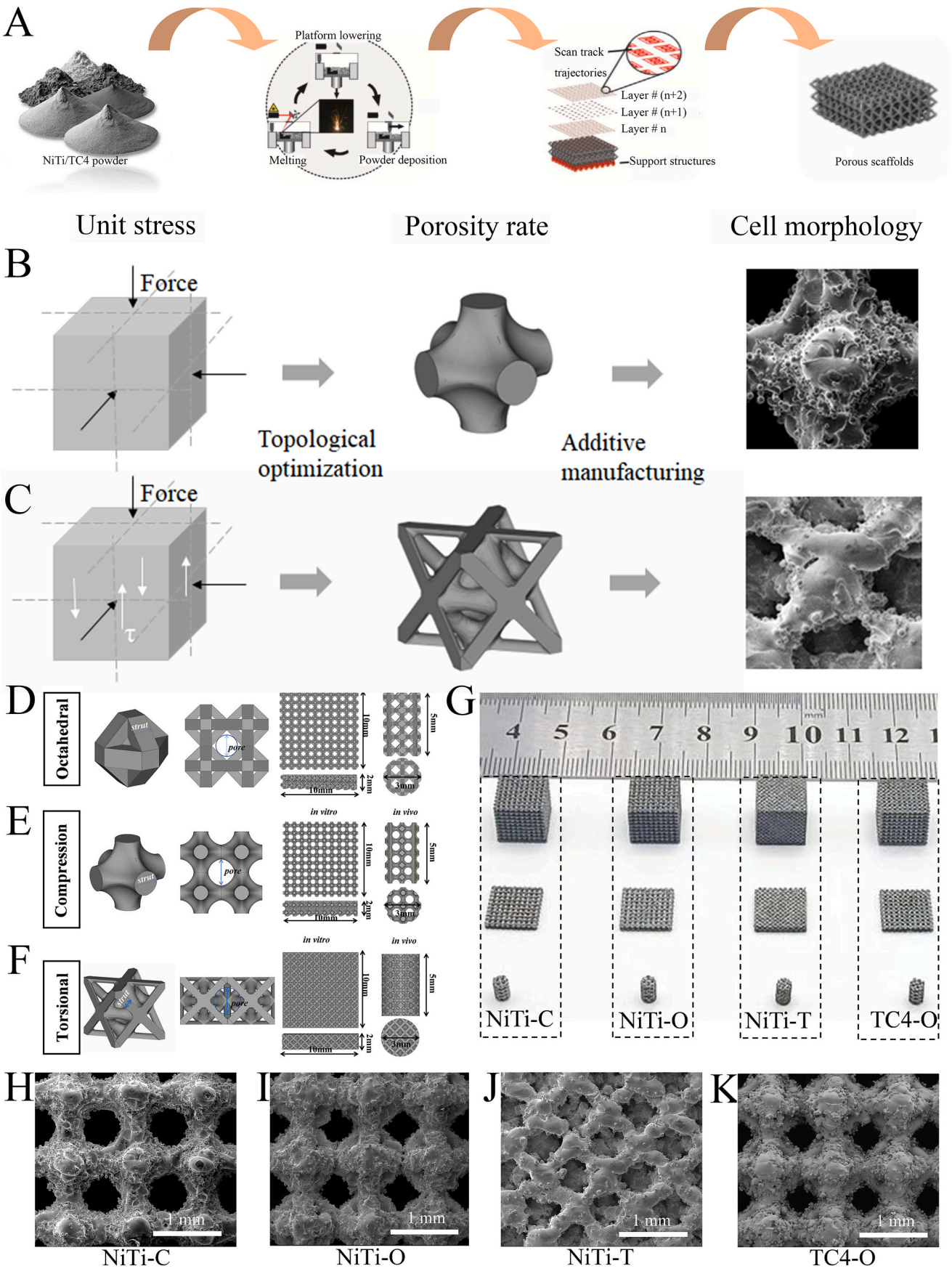

(caption on next page)

Fig. 1. The design and LPBF fabrication of NiTi alloy porous scaffolds. A: The flowchart depicting the fabrication process of the scaffolds. B and C: The process of porous structure topology optimization, including the finite element physical model and boundary conditions for both compression-type and torsion-type unit cells. This is followed by the models after topology optimization for these unit cells, as well as the LPBF-processed topologically optimized versions. D–F: Three types of cellular structures: the traditional octahedral type (D), the topologically optimized compression type (E), and the torsion type (F), accompanied by schematic diagrams of the corresponding porous scaffolds. G: LPBF-processed NiTi alloy porous scaffolds, featuring compression, octahedral, and torsion cell structures, were compared to a titanium alloy (Ti-6Al-4V) porous scaffold with an octahedral cell structure, which served as the control group. The dimensions of the porous scaffold utilized for in vitro biological experiments were 10 mm × 10 mm × 2 mm. For in vivo animal experiments, the cylindrical porous scaffold measured φ3 mm × 5 mm, while the cubic porous scaffold employed for physical performance tests was 10 mm × 10 mm × 10 mm in size. H–K: SEM observation of the porous scaffolds, a compression-type NiTi alloy porous scaffold (NiTi-C)(H), an octahedral-type NiTi alloy porous scaffold (NiTi-O)(I), a torsion-type NiTi alloy porous scaffold (NiTi-T)(J) and an octahedral-type titanium alloy porous scaffold (TC4-O)(K), respectively (scale bars = 1 mm).

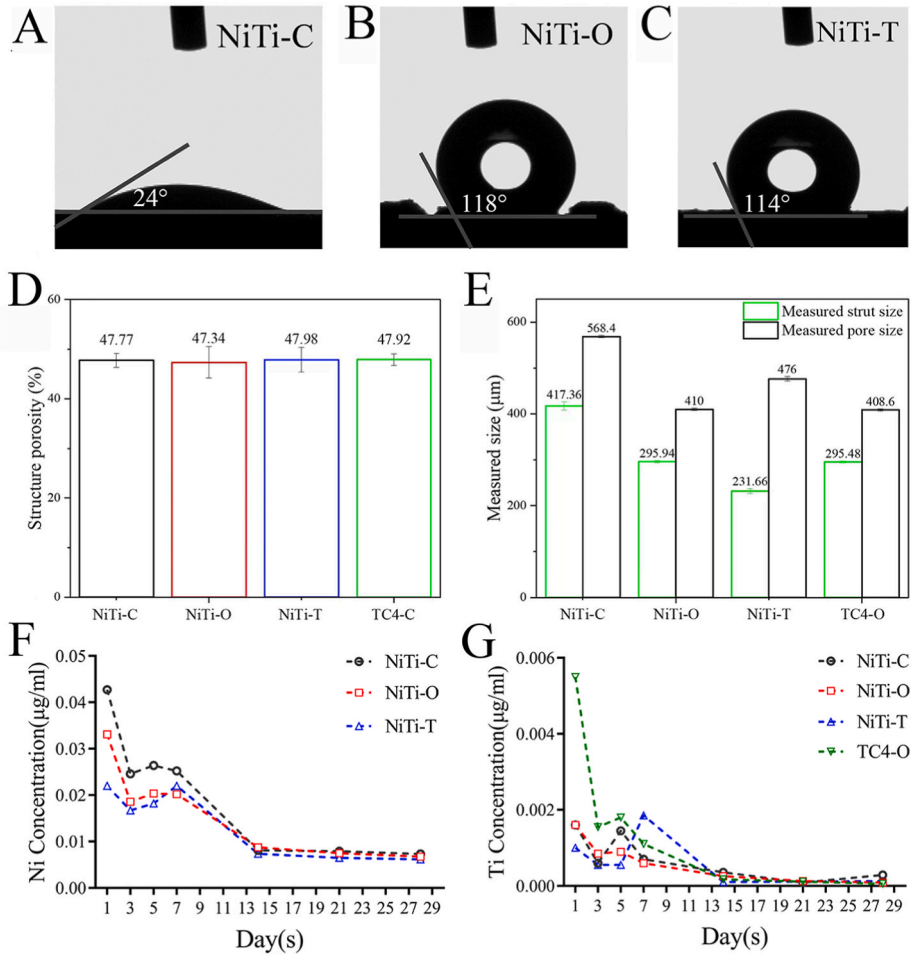

Fig. 2. The physical properties of NiTi alloy porous scaffolds. A–C: The water contact angles of NiTi alloy porous scaffolds with varying cellular structures. D: The structural porosities of the porous scaffolds. E: The strut sizes and pore sizes of the different porous scaffolds. F and G: Ion release of the porous scaffolds under simulated physiological fluids, including the nickel ion release curves of the porous NiTi scaffolds (F) and the release curves of titanium ions from NiTi-C, NiTi-O, NiTi-T, and TC4-O porous scaffolds (G). All statistical data are represented as mean ± SD (n = 3).

threshold, the contact angle decreases sharply, resulting in improved hydrophilicity.

The nickel ion release curves of the porous NiTi scaffolds are illustrated in Fig. 2F. The concentration of nickel ions released by the three cellular scaffolds was observed to range from high to low in the following order: NiTi-C, NiTi-O, and NiTi-T. This variation may be attributed to the permeability associated with the type of unit cell structure. Enhanced permeability facilitates better infiltration and fluidity, resulting in a greater release of ions. Furthermore, there exists an indirect relationship between permeability and biological effects, which aligns with the findings of the biological studies conducted in this research. Nickel ions were predominantly released during the first week, followed by a rapid decline, ultimately reaching a stable low-level precipitation state over the final three weeks. The reduction in nickel ion release may be linked to the formation of a titanium oxide layer on the surface of the nickel-titanium alloy [42]. It has been demonstrated that NiTi readily undergoes passivation, forming a TiO2 surface layer similar to that of pure titanium, thereby confining nickel release to the initial days when such materials are immersed in vitro [43–45]. This abrupt decrease within a short timeframe may help mitigate a continuous state of acute inflammation in the body post-implantation, thereby promoting the integration of the implant with the bone interface and enhancing bone ingrowth. Fig. 2G illustrates the release curves of titanium ions from NiTi-C, NiTi-O, NiTi-T, and TC4-O porous scaffolds. Although their precipitation trends are similar, the porous titanium alloy scaffolds exhibit a higher release of titanium ions compared to the porous NiTi alloy scaffolds during the first week. Concerns regarding the safety of nickel ion release are prevalent in the context of NiTi alloy applications.

Indeed, there are established requirements and standards governing the safe concentration of nickel ions [46–50]. Consequently, NiTi alloy implants produced through various manufacturing processes will be evaluated against these standards to ensure the safety of nickel ion release. Numerous in vitro and in vivo studies have demonstrated the reliable performance of nickel ion release from implants derived from their respective manufacturing processes across multiple service environments [20,22,27,51,52]. The concentrations of nickel ions released from the three types of porous NiTi alloy scaffolds with distinct cellular structures in this study complied with the aforementioned release standards. Many researchers have sought to further minimize nickel ion release through surface modification techniques, achieving satisfactory results [20,53–56]. Future research directions may focus on surface modifications tailored to specific functional requirements.

Fig. 3A presents the XRD curves of various NiTi porous scaffolds, with XRD measurements conducted at a room temperature of 26 °C. The XRD results indicate that the predominant phase in these scaffolds is the B2 austenite phase, accompanied by a minor presence of B19' martensite. Fig. 3B illustrates the phase transformation process during the heating and cooling of the different NiTi porous scaffolds. Typically, porous scaffolds are cooled from a high temperature to a lower temperature during their formation. This observation suggests that the three NiTi porous scaffolds contain a small amount of B19' martensite, as indicated by the cooling curve, which aligns with the XRD findings. Subsequent animal experiments will be performed on SD rats, which are endothermic animals with an internal temperature of approximately

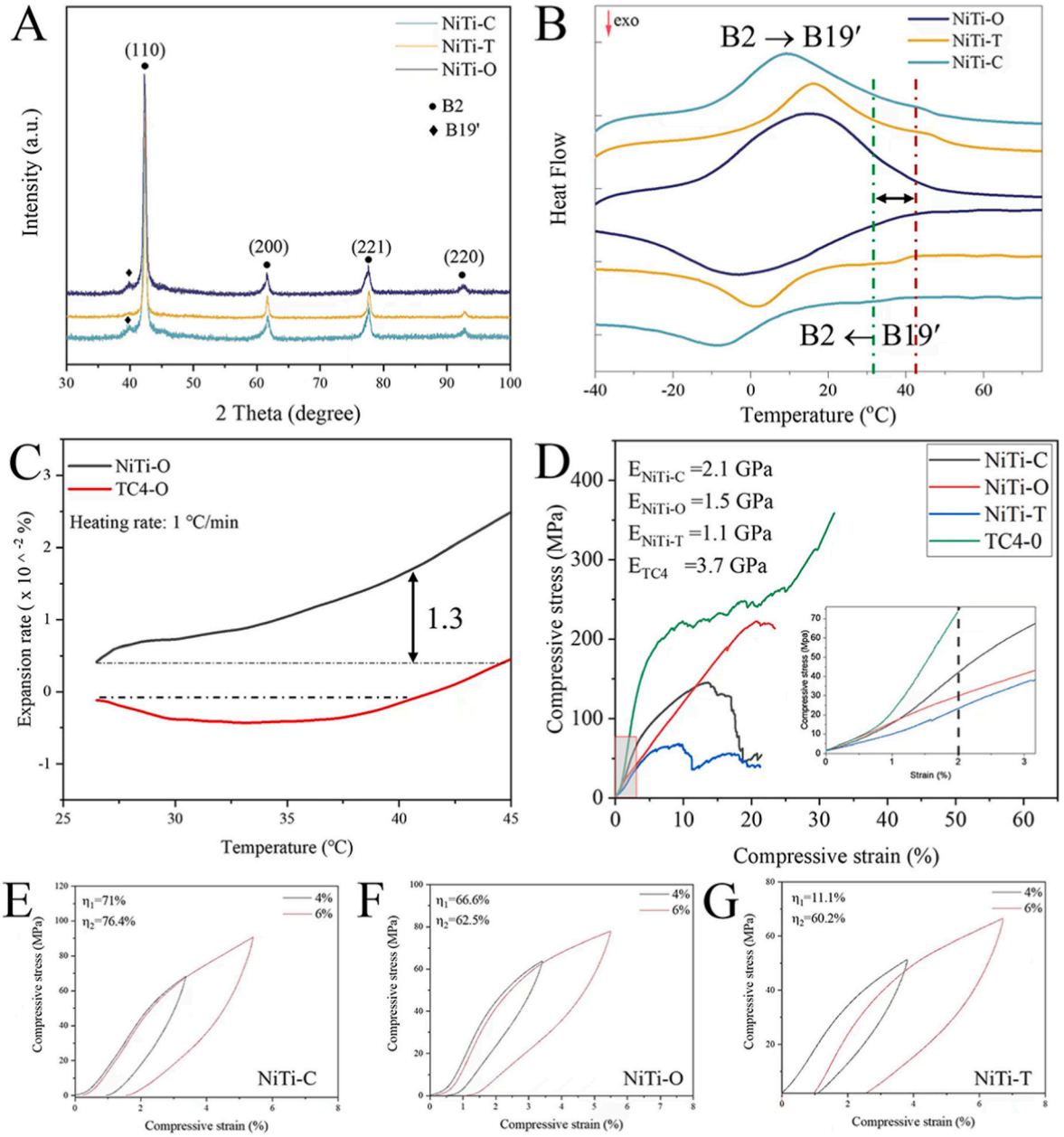

Fig. 3. The compression test and functional characteristic test of NiTi alloy porous scaffolds. A: The X-ray diffraction (XRD) curves of various NiTi porous scaffolds, with XRD measurements conducted at a room temperature of 26 °C. B: The phase transformation process during the heating and cooling of the different NiTi porous scaffolds. C: The linear expansion rates of NiTi-O and TC4-O. D: The mechanical properties of different porous scaffolds (elasticity modulus). E–G: The thermo-mechanical curves, with all three sets of curves demonstrating the superelasticity and shape memory effects of NiTi-C (E), NiTi-O (F), and NiTi-T (G) porous scaffolds, respectively. These effects are attributed to the test temperature being within the phase transition temperature range for NiTi alloys. The η in the figures display the heat recovery rates for each test.

41 °C. The Differential Scanning Calorimetry (DSC) results reveal that martensite transforms into austenite in all three NiTi porous scaffolds within the temperature range of 26–41 °C as the temperature increases, indicating a notable volume expansion. Excluding the influence of cellular structure type, the linear expansion rates of NiTi-O and TC4-O were further evaluated (Fig. 3C). The results show that the linear expansion of NiTi-O is approximately 1.3 x 10ˆ2% as the temperature rises to 41 °C, while the linear expansion of TC4-O remains relatively unchanged. This difference is attributed to the unique phase transition mechanism of the NiTi alloy. Fig. 3D illustrates the mechanical properties of various porous scaffolds, with their corresponding elasticity moduli indicated as 2.1 GPa, 1.5 GPa, 1.1 GPa, and 3.7 GPa, respectively. Notably, the NiTi-T scaffold exhibits the lowest modulus, while the TC4-O scaffold shows the highest. The elastic modulus of the NiTi alloy porous scaffolds is comparable to that of cancellous bone [22,57]. A closer match between the elastic modulus of the porous scaffold and that of bone can effectively mitigate issues such as stress shielding, cutting, and sinking in orthopedic applications [1]. Fig. 3E, F and G present the thermomechanical curves for NiTi-C, NiTi-O, and NiTi-T, respectively. All three sets of curves demonstrate the superelasticity and shape memory effects of NiTi alloy porous scaffolds, attributed to the test temperature being within the phase transition temperature range for NiTi alloys [26]. The η in the figures display the heat recovery rates for each test. The heat recovery rates for NiTi-C were recorded at 71 % and 76.4 %, for NiTi-O at 66.6 % and 62.5 %, and for NiTi-T at 11.1 % and 60.2 %, respectively. It was observed that the memory effect of NiTi-C was the most pronounced, which is primarily related to its design configuration.

Fig. 4 presents the micro-CT 3D reconstruction models and internal defect images of the NiTi-C, NiTi-O, NiTi-T, and TC4-O porous scaffolds. The reconstructed models were compared with the designed CAD models to intuitively and quantitatively assess the degree of deviation. Observations indicated both positive and negative deviations on the surface of the porous NiTi alloy scaffold (Fig. 4A–D, G, and J). In conjunction with the SEM surface microscopic results of the scaffolds, we propose that post-treatment methods, such as sandblasting following molding, could mitigate most positive deviations in future studies. The micro-CT reconstruction model was superimposed with the CAD model to ascertain the dimensional deviation, as illustrated in Fig. 4C–F, I, and L. The average deviations for the NiTi-C, NiTi-O, NiTi-T, and TC4-O porous scaffolds were measured at 0.013 mm, 0.015 mm, 0.016 mm, and 0.025 mm, respectively. These results indicate that the porous NiTi

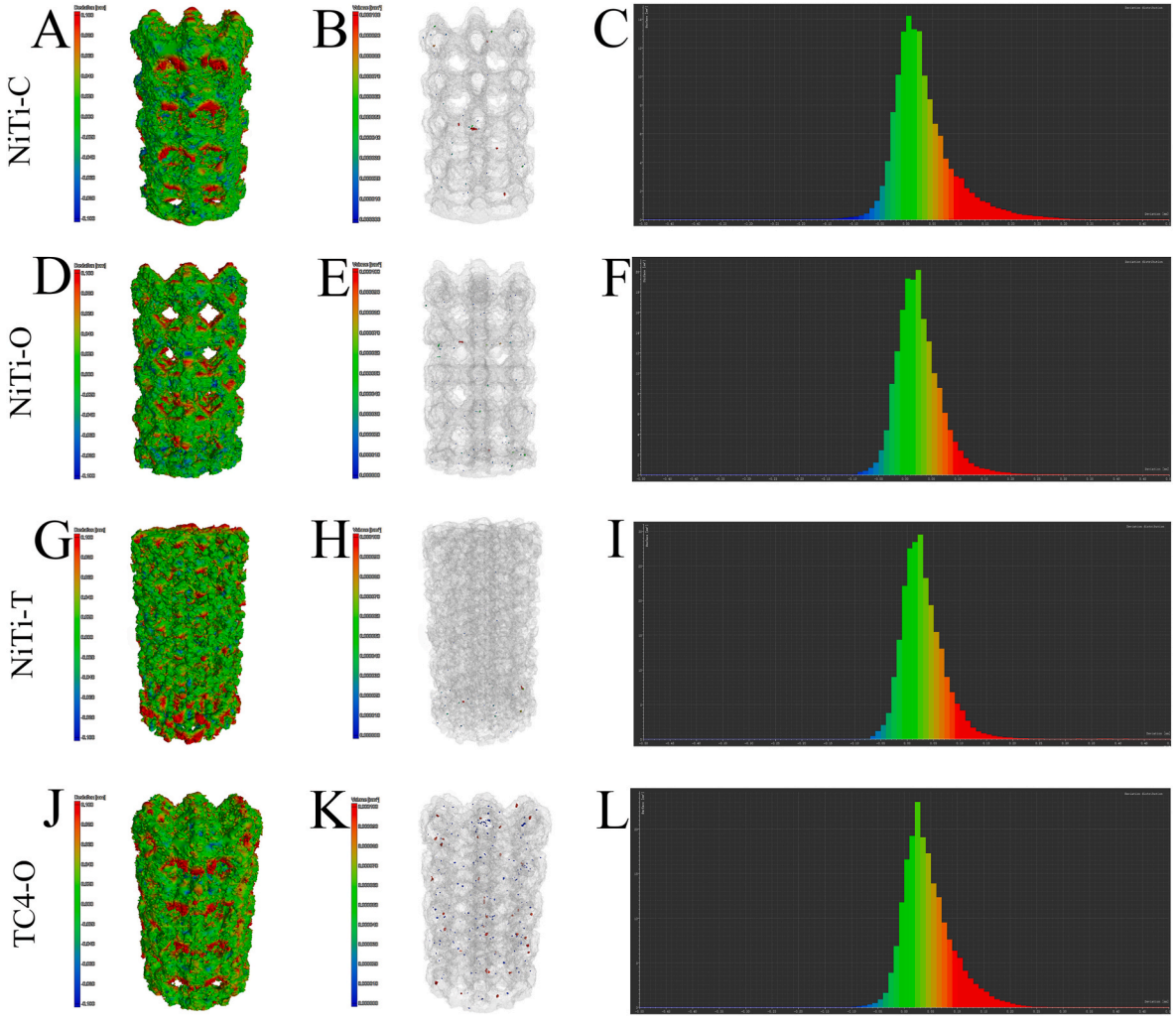

Fig. 4. The Micro-CT 3D reconstruction models and internal defect images of the NiTi-C, NiTi-O, NiTi-T, and TC4-O porous scaffolds following LPBF molding, with the cylindrical porous scaffold measuring φ3 mm × 5 mm. A, D, G and J: The Micro-CT 3D reconstruction models, highlighting both positive and negative surface deviations of the porous NiTi alloy scaffold. B, E, H and K: The reconstructed internal defect images demonstrated that the defects were uniformly distributed throughout the porous NiTi alloy scaffold. C, F, I and L: The micro-CT reconstruction model was superimposed with the CAD model to ascertain the dimensional deviation. The average deviations for the NiTi-C(C), NiTi-O(F), NiTi-T(I), and TC4-O(L) porous scaffolds were measured at 0.013 mm, 0.015 mm, 0.016 mm, and 0.025 mm, respectively.

alloy scaffolds produced in this study closely resemble the designed CAD models. Additionally, the internal defect images demonstrated that the defects were uniformly distributed throughout the porous NiTi alloy scaffold (Fig. 4B–E, H, and K). During the LPBF formation process, the temperature of the molten pool increases rapidly as the laser melts the powder. When this temperature exceeds the boiling point, Ni and Ti atoms begin to evaporate. Specifically, the boiling points of Ni and Ti are 3003 K and 3560 K, respectively. Consequently, because Ni has a significantly lower boiling point, its evaporation will dominate once the temperature surpasses that threshold. Simultaneously, during the rapid solidification of the molten metal, water vapor can be entrapped, resulting in the formation of micropores or smaller defects [58]. Previous studies have confirmed the occurrence of Ni evaporation in LPBF NiTi alloy samples [59]. These factors contribute to the internal defects observed in NiTi alloy scaffolds. However, the low defect rate reported in this study indicates that the LPBF process parameters employed are suitable for the manufacturing of porous NiTi alloy scaffolds.

3.3. Biocompatibility of porous NiTi alloy scaffolds

Fig. 5A illustrates that the four types of porous scaffolds, characterized by distinct cellular structures, exhibit significant protein adsorption capacities. Notably, the NiTi-T porous scaffold, which possesses the largest surface area, demonstrated the highest protein adsorption within a 24-h period. The protein adsorption capacity of these scaffolds substantially influences the activity of cells on their surfaces; specifically, enhanced protein adsorption correlates with improved cell adhesion and proliferation [60]. rBMSCs were inoculated onto both porous NiTi alloy and porous titanium alloy scaffolds and subsequently cocultured. Live and dead cell staining was conducted after 3 and 7 days of coculture. The findings indicated that rBMSCs effectively spread and proliferated on all four types of porous scaffolds after 3 days (Fig. 5C). By the 7-day mark, rBMSCs had proliferated and covered the entirety of the porous scaffold (Fig. 5D).

Additionally, rBMSCs were cultured in media prepared with extracts from the four types of porous scaffolds. The negative control group was maintained on complete cell culture medium. Live and dead cell staining was performed at both 3 days (Fig. S2) and 7 days (Fig. S3) of culture. The results indicated that the growth and proliferation of rBMSCs were comparable to those observed in the negative control group, while the positive control group, which was supplemented with DMSO in the culture medium, exhibited significant toxicity. The CCK-8 assay assessed cell proliferation and revealed a favorable growth trend, with proliferation activity comparable to that of the negative control group. In contrast, the porous scaffolds demonstrated good biocompatibility when compared to the positive control group (Fig. 5B).

After the porous scaffolds were cocultured with the rBMSCs for 7 days, the cytoskeleton and cell nucleus were examined using a laser confocal scanning microscope, revealing satisfactory cell growth (Fig. 5E). SEM was employed to assess cell adhesion and growth on the scaffolds, and the results indicated that the rBMSCs adhered to and spread effectively after 7 days of culture on each type of porous scaffold (Fig. 5F). No significant differences in cell morphology, size, or number were observed among the four types of porous scaffolds. Regarding the LPBF process, the complex cellular structure samples with stress-based topological optimization demonstrated superior biocompatibility compared to other dense samples [61] and porous samples with conventional simple cellular structures [27–29]. The biocompatibility of NiTi alloy implants produced through traditional manufacturing processes has been validated according to international standards (ISO) [62–65]. Both in vivo and in vitro biocompatibility studies have confirmed that the NiTi alloy fulfills the requirements and criteria for implantation [19–21,66,67].

3.4. In vitro osteogenic properties of porous NiTi alloy scaffolds

rBMSCs were cultured in media prepared with extracts from four types of porous scaffolds, and ALP staining was conducted after 7 and 14 days of osteogenic induction (Fig. 6A and B). The quantitative assessment of ALP activity indicated that both the NiTi alloy porous scaffold and the titanium alloy porous scaffold effectively facilitated the differentiation of rBMSCs into bone, with ALP activity significantly exceeding that of the control group. However, there was minimal variation in ALP activity among the different porous scaffold groups (Fig. 6E).

Furthermore, we evaluated the osteogenic mineralization capacity of the four types of porous scaffolds. The experimental group settings and processing conditions were consistent with those described previously. After 14 and 21 days of osteogenic induction, the mineralized nodules were stained using Alizarin Red S dye (Fig. 6C and D). Quantitative analysis following the dissolution of the mineralized nodules indicated that both the porous NiTi alloy scaffold and the titanium alloy porous scaffold exhibited a notable ability to catalyze mineralized nodule formation, significantly surpassing that of the control group (Fig. 6F). At 14 days, there was minimal difference in mineralization capacity among the porous scaffold groups; however, by 21 days, the NiTi-T porous scaffolds demonstrated superior mineralized nodule formation compared to the TC4-O porous scaffolds. Similarly, ALP activity of cells cultured on porous NiTi alloy samples produced via temporary spaceholder (NH4HCO3) and conventional sintering methods was higher than that observed in pure titanium metal samples [19].

rBMSCs were cocultured with four types of porous scaffolds. After 7 and 14 days of osteogenic induction, RT−PCR was performed to detect the expression of osteogenic-related genes, including OPN (Fig. 7A), RunX2 (Fig. 7B), Col-1 (Fig. 7C), and OCN (Fig. 7D). The results indicated that, in the osteogenic induction medium cocultured with porous scaffolds, the expression of these genes increased to varying degrees and was significantly higher than that observed in the control group; however, there was minimal difference among the porous scaffold groups. Protein immunoblotting experiments corroborated these findings (Fig. 7E and F). The NiTi alloy and titanium alloy porous scaffolds effectively enhanced in vitro osteogenic efficiency in the short term. Compared to the control polystyrene plate, the ALP activity and osteogenic mineralization ability of the 70 % porous NiTi alloy scaffolds, produced via powder immersion reaction assisted coating (PIRAC) conversion (titanization) using the nickel foam method, were superior [20]. Furthermore, in a coculture system of microvascular endothelial cells and mesenchymal stem cells, the formation of prevascular structures within NiTi alloy trabecular scaffolds was experimentally demonstrated [20], which may serve as an important prerequisite for effective osteogenesis in vivo. Numerous in vitro studies have shown that NiTi alloy scaffolds can promote bone differentiation under osteogenic induction [28] or mechanical force stimulation [29]. The results from the in vitro osteogenesis experiments in this study were consistent with those of previous studies, further demonstrating the significant potential application of NiTi alloy scaffolds in the field of bone repair.

3.5. In vivo bone ingrowth performance of porous NiTi alloy scaffolds

NiTi-C, NiTi-O, NiTi-T, and TC4-O porous scaffolds were implanted into the bone defect located in the distal lateral condyle of the femurs of SD rats. Fig. 8A illustrates the general process and implantation position of the porous metal scaffold in vivo.

Fig. 8B and C presents the micro-CT images of the longitudinal and transverse sections of each scaffold after four and twelve weeks of implantation, respectively. The porous scaffolds maintained close contact with the bone interface, and new bone developed from the bone contact surface surrounding the scaffold, extending along the pores into the porous scaffold and resulting in trabecular structures with varying numbers and thicknesses.

By marking the scaffold structure in yellow and the bone ingrowth

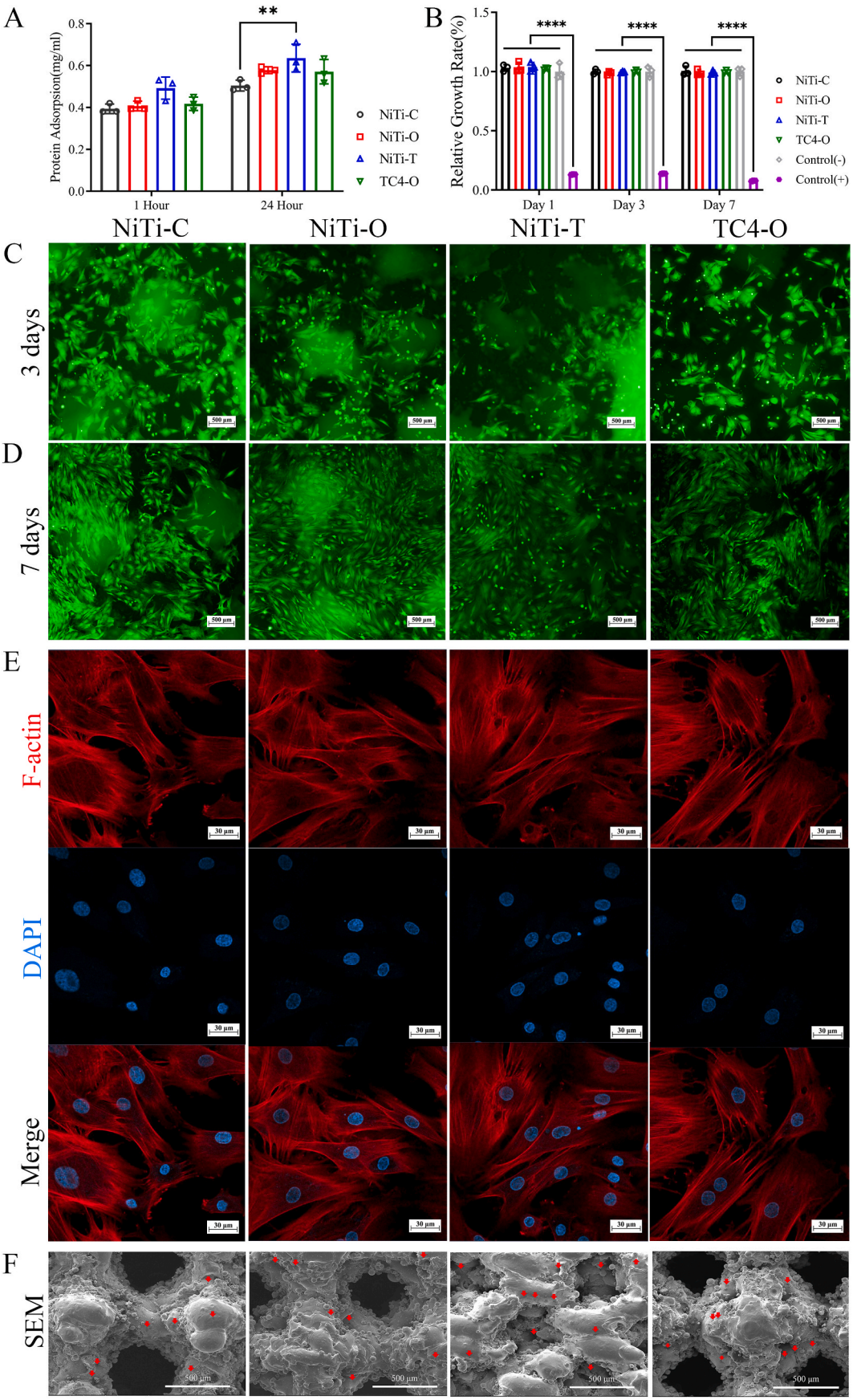

(caption on next page)

Fig. 5. The coculture of rat bone marrow mesenchymal stem cells (rBMSCs) with porous scaffolds, along with microscopic observation images. A: The protein adsorption experiment, where the four types of porous scaffolds, each characterized by distinct cellular structures, demonstrate significant protein adsorption capacities. B: The results of the CCK-8 assay, which assessed cell proliferation and indicated a favorable growth trend. C: Live/dead staining fluorescence image of cells on the surface of the porous alloy scaffolds after 3 days of coculture, revealing that rBMSCs effectively spread and proliferated on all four types of porous scaffolds (scale bars = 500 μm). D: Live/dead staining fluorescence image of cells on the surface of the porous alloy scaffolds after 7 days of coculture, indicating that rBMSCs had proliferated and covered the entire surface of the porous scaffold (scale bars = 500 μm). E: The cytoskeleton and cell nucleus using a laser confocal scanning microscope after 7 days of coculture with rBMSCs, reveals satisfactory cell growth (scale bars = 30 μm). F: Scanning electron microscopy to assess cell adhesion and growth on the scaffolds (scale bars = 500 μm). All statistical data are represented as mean ± SD (n = 3; **P < 0.01, ****P < 0.0001).

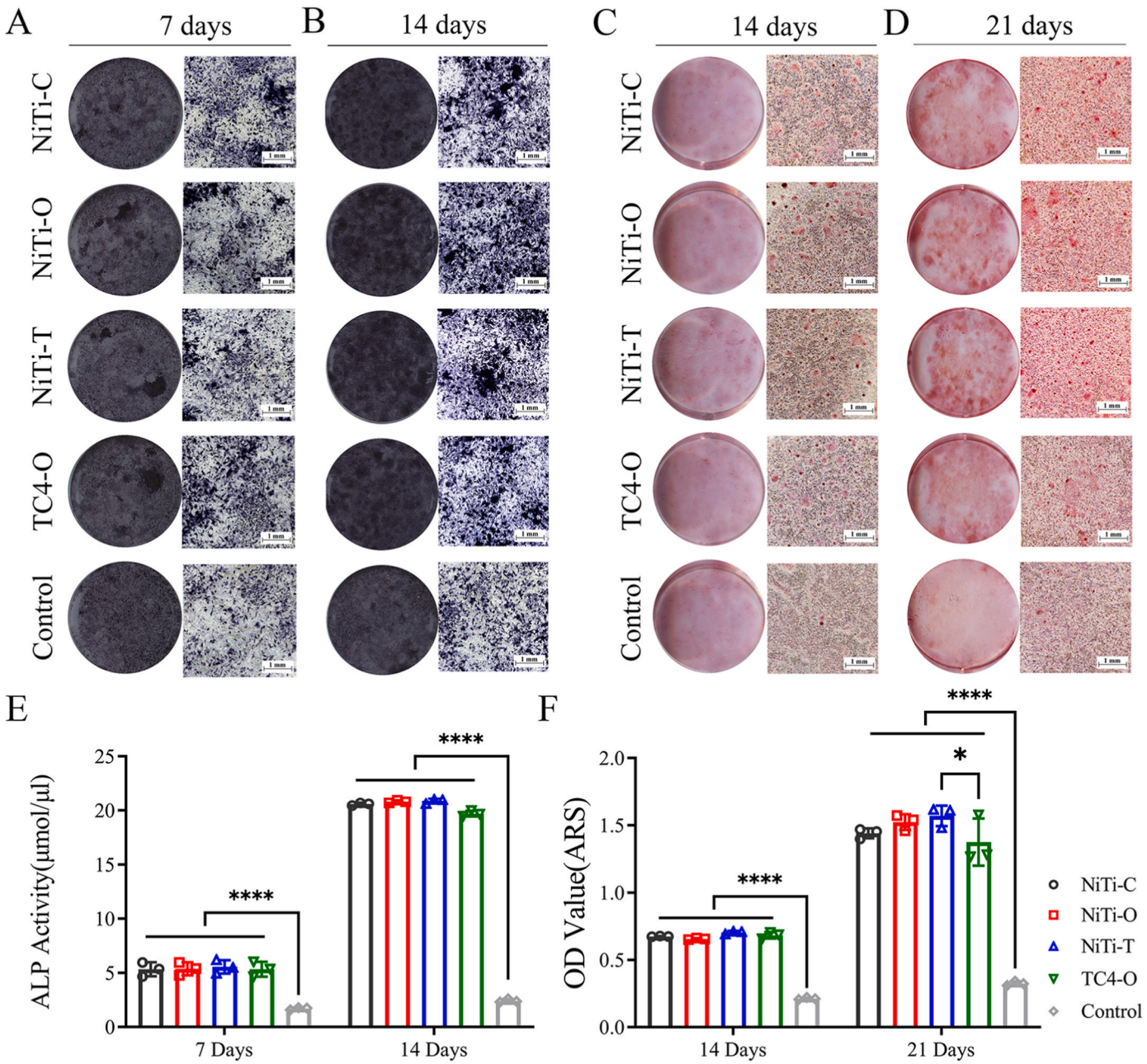

Fig. 6. In vitro alkaline phosphatase (ALP) activity and osteogenic mineralization ability of porous scaffolds. A and B: rBMSCs were cultured in media prepared with extracts from four types of porous scaffolds, with ALP staining performed after 7 and 14 days of osteogenic induction (scale bars = 1 mm). C and D: The mineralized nodules were stained using Alizarin Red S dye after 14 and 21 days of osteogenic induction (scale bars = 1 mm). E: Quantitative ALP activity detection; F: Quantitative detection of mineralized nodules. All statistical data are represented as mean ± SD (n = 3; *P < 0.05, ****P < 0.0001).

structure in red, the visualization of new bone growth is enhanced. At four weeks post-implantation, the new bone began to make contact with the scaffold from all sides, grew within the porous scaffold, and extended into the shallower pores (Fig. 8D). By twelve weeks post-implantation, the new bone advanced into the deeper regions of the porous structure, ultimately filling all of the pores (Fig. 8E). Fig. S4 highlights the new bone in red over a transparent scaffold structure, providing a clearer representation of the bone ingrowth process.

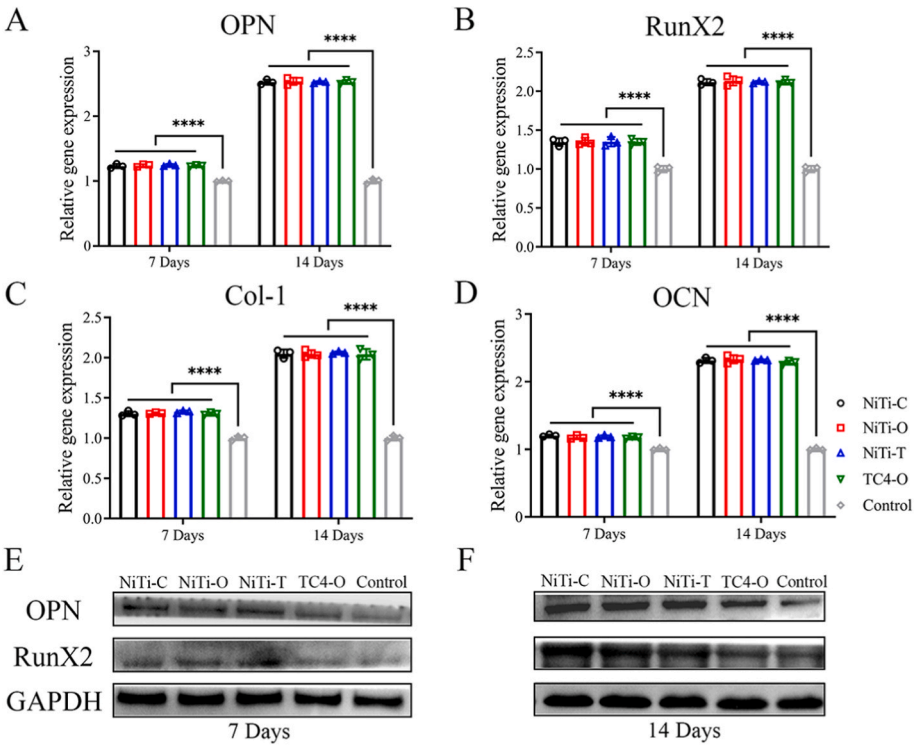

Fig. 7. In vitro osteogenic efficiency-related gene expression detection of porous scaffolds. A–D: rBMSCs were cocultured with four types of porous scaffolds. After 7 and 14 days of osteogenic induction, RT−PCR was performed to detect the expression of osteogenic-related genes, including OPN (A), RunX2 (B), Col-1 (C), and OCN (D). E and F: Western blotting assay used to detect osteogenic-related proteins. All statistical data are represented as mean ± SD (n = 3; ****P < 0.0001).

Osteometric analysis of the micro-CT data revealed that the new bone volume/total volume (BV/TV%) of the NiTi-O and NiTi-C porous scaffolds was greater than that of the TC4-O porous scaffolds at four weeks post-implantation. At twelve weeks post-implantation, all three types of NiTi alloy porous scaffolds exhibited greater BV/TV% compared to the TC4-O scaffolds, with the NiTi-C porous scaffolds demonstrating the highest new bone volume (Fig. 8F). Additionally, the number of new bone trabeculae (Fig. 8G) in the NiTi-C and NiTi-T porous scaffolds increased compared to that in the TC4-O porous scaffolds at both four and twelve weeks post-implantation. Among the three types of NiTi alloy porous scaffolds, the NiTi-T exhibited the most bone trabeculae at four weeks, likely due to its greater number of pores. However, by twelve weeks post-implantation, no significant difference was observed between the NiTi-C and NiTi-T porous scaffolds. Regarding the thickness of the newly formed trabecular bone (Fig. 8H), at the initial stage of implantation, the NiTi-O and NiTi-C porous structures were thicker than the TC4-O scaffolds; however, this difference became insignificant at twelve weeks. Among the three types of porous NiTi alloy scaffolds, the NiTi-O and NiTi-C scaffolds with larger interconnected pores exhibited thicker trabecular bone. Based on these three indicators, the bone ingrowth efficiency of the porous NiTi alloy scaffolds is superior to that of the porous titanium alloy scaffolds. Furthermore, the NiTi-C porous scaffolds demonstrated better bone ingrowth performance compared to the NiTi-O and NiTi-T scaffolds.

The tissue samples obtained after in vivo implantation were sliced along with the metal scaffolds to further evaluate bone ingrowth. Fig. 9A and B present longitudinal sections and locally magnified images of each scaffold at four weeks and twelve weeks post-implantation. Methylene blue-acid magenta stain was employed to color the new trabecular bone structure red. The new trabecular bone, which developed from the periphery of the scaffold toward the interior of the porous structure, exhibited varying shapes and thicknesses and was either continuous or segmented. This variability reflects the guiding role of different cellular structures in directing the growth of new bone along the pore direction. The results of the in vivo animal experiments in this study demonstrated that porous scaffolds with varying cellular structures exhibit distinct guiding effects on the ingrowth of new bone. Biomimetic structural strategies are increasingly employed in tissue engineering to facilitate cell migration and bone ingrowth [68,69]. Scaffolds with different spatial topologies may influence the behaviors of multiple cell types. Notably, the NiTi-C porous scaffolds showed superior bone ingrowth performance compared to both NiTi-O and NiTi-T porous scaffolds, likely due to the enhanced permeability of compression-type porous scaffolds. In terms of biological performance, the permeability of porous scaffolds is a critical parameter that reflects the scaffold's overall characteristics, including pore shape, pore size, pore connectivity, pore distribution, and scaffold area [70,71]. These factors significantly impact the dispersion and exchange of nutrients and oxygen within the porous scaffold [72], cell seeding efficiency [73,74], in vitro 3D culture [75,76], and ultimately the formation of bone tissue in vivo [77,78]. Research has indicated that varying pore structures within porous scaffolds create different forms of pore connections and channels with distinct tortuosities, leading to variations in permeability even among scaffolds with identical porosity and pore size [79]. High-permeability scaffolds can enhance the ingrowth and vascularization of bone tissue [80]. Furthermore, NiTi-C exhibits a higher heat recovery rate among NiTi alloy porous scaffolds, which may also contribute to the improved bone ingrowth efficiency observed in this type of cellular structure.

Goldner's trichrome-stained tissue sections further illustrated the process of new bone trabeculae growing into the porous structure (Fig. 9C and D). Quantitative analysis of the new bone ingrowth area within the porous scaffold (Fig. 9E) indicated that, at four weeks post-implantation, the NiTi-C porous scaffolds exhibited a larger new bone area compared to the TC4-O porous scaffolds. At twelve weeks post-implantation, the three types of NiTi alloy porous structures demonstrated superior new bone ingrowth effects relative to the titanium alloy, with the NiTi-C porous scaffolds showing the largest bone area. Regarding the bone contact area between porous scaffolds and bone

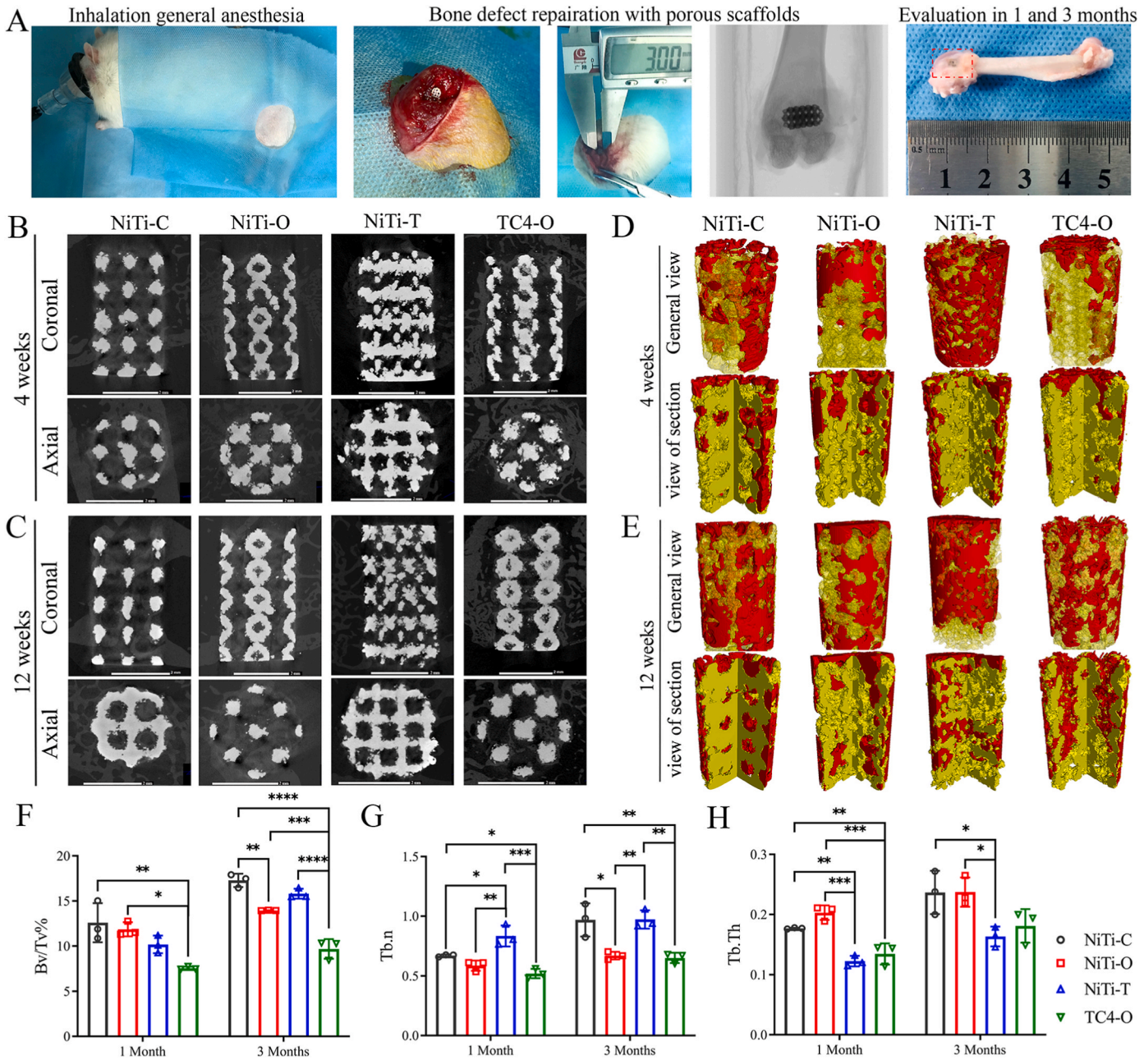

Fig. 8. Micro-CT images of both longitudinal and transverse sections of porous scaffolds following implantation, as well as an analysis of new bone growth within the porous structure and bone metrology. A: The general process and the implantation position of the porous metal scaffold in vivo. B and C: The micro-CT images of the longitudinal and transverse sections of each scaffold after four(B) and twelve(C) weeks of implantation (scale bars = 2 mm). D and E: By marking the scaffold structure in yellow and the bone ingrowth structure in red, the visualization of new bone growth is enhanced. At four weeks post-implantation, the new bone began to make contact with the scaffold from all sides, grew within the porous scaffold, and extended into the shallower pores (D). By twelve weeks post-implantation, the new bone advanced into the deeper regions of the porous structure, ultimately filling all of the pores (E). The cylindrical porous scaffold measured φ3 mm × 5 mm. F: New bone volume/total volume (BV/TV%); G: The number of new bone trabeculae; H: The thickness of the newly formed trabecular bone. All statistical data are represented as mean ± SD (n = 3; *P < 0.05, **P < 0.01, ***P < 0.001, ****P < 0.0001).

(Fig. 9F), no significant differences were observed among the four types of porous scaffolds at the two observation time points, suggesting that both NiTi alloy and titanium alloy porous scaffolds can integrate effectively with the bone interface, facilitating successful bone fusion. The bone contact area analysis revealed that both the NiTi alloy and titanium alloy porous scaffolds exhibit strong integration with the bone interface, facilitating effective osseointegration. However, the bone ingrowth efficiency of the porous NiTi alloy scaffold surpasses that of the porous titanium alloy scaffold. This advantage of the NiTi alloy scaffolds may be attributed to the volume expansion effect resulting from phase transformation. Specifically, the NiTi scaffolds were heated from room temperature to the body temperature after implantation, leading to a significant expansion effect compared to the titanium scaffolds. This volume expansion allows the NiTi scaffolds to be in closer proximity to the bone interface. Furthermore, the elastic modulus of NiTi porous scaffolds is relatively low, aligning closely with that of cortical bone, which may facilitate the generation of a continuous and appropriate force during the expansion process. This phenomenon could significantly contribute to enhanced bone ingrowth. Similarly, porous NiTi alloy implants produced through conventional manufacturing processes

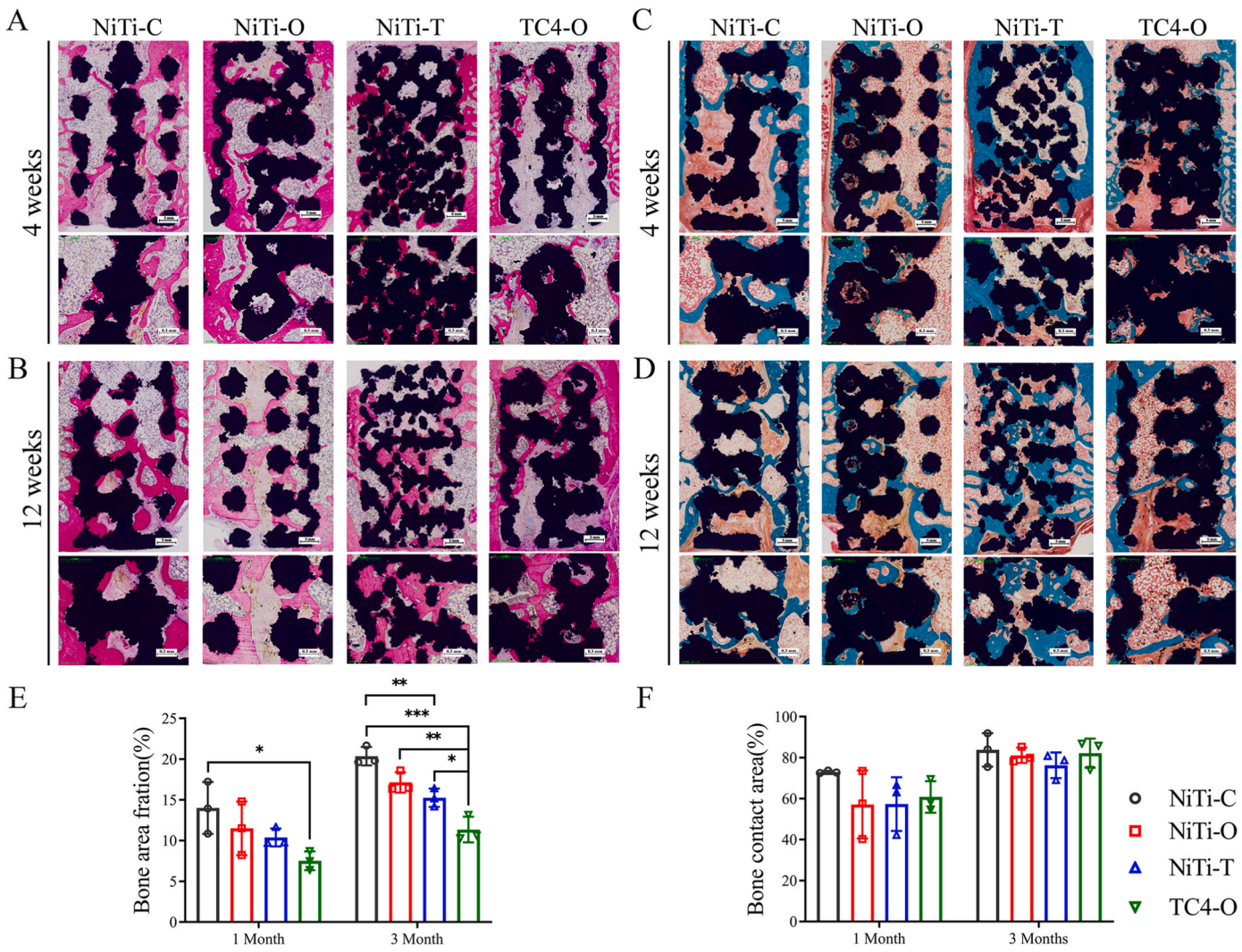

Fig. 9. Images of methylene blue-acid magenta staining and Goldner's trichrome staining of tissue sections at four weeks and twelve weeks post-implantation of each scaffold. A and B: Longitudinal sections and locally magnified images of each scaffold at both time points. C and D: Longitudinal sections and locally magnified images of Goldner's trichrome staining of tissue sections at both time points. E: Quantitative analysis of the new bone ingrowth area within the porous scaffold. F: The bone contact area between the porous scaffolds and bone. All statistical data are represented as mean ± SD (n = 3; *P < 0.05, **P < 0.01, ***P < 0.001). (scale bars of longitudinal sections = 5 mm, scale bars of locally magnified images = 0.3 mm).

demonstrated superior osseointegration compared to Ti-6Al-4V cages, exhibiting even better osseointegration quality [24]. Moreover, porous NiTi alloys manufactured via traditional methods also displayed rapid bone growth [22], comparable to the effectiveness of hydroxyapatite [23]. Furthermore, porous NiTi alloy scaffolds produced through self-propagating high-temperature synthesis (SHS) exhibited commendable bone ingrowth performance as evidenced by pathological sections [81], showed a lower incidence of fibrosis [82], and presented a high bone ingrowth rate (78.3 ± 9.7 %) even at an early stage (6 weeks post-implantation) [83].

The objective of identifying the optimal unit cell structure is to enhance early bone integration and improve the strength of bone integration within an environment that aligns with the local biomechanical requirements of the human body. This study employed a porous structure topology optimization method, informed by the actual stress state of human bones, to refine the porous structural unit. In vivo and in vitro experiments demonstrated that the LPBF NiTi alloy porous scaffold, based on the predominant cellular structure, exhibits satisfactory osteogenic efficiency. Currently, most customized bone repair prostheses are constrained in their ability to tailor anatomical morphology. This study offers a significant reference for clinical practice, indicating that topological optimization of cellular structures can be performed according to varying body regions and distinct in vivo stress characteristics, thereby enabling the realization of clinically personalized prostheses with topologically optimized dominant cellular structures.

These findings lay a robust preliminary experimental foundation for the clinical application of NiTi alloy scaffolds, which possess favorable bionic mechanical properties and deformable capabilities for the dynamic repair of bone defects. Furthermore, this study underscores the importance of personalized customization in mechanical adaptations within clinical practice. However, a limitation of this study is that the design of the animal experiments did not adequately assess deformation effects, which represents a frontier for future research. Additionally, it will be essential to conduct large animal experiments to validate these customized bone repair prostheses and to complete their preclinical verification in the future.

4. Conclusions

NiTi alloy porous scaffolds can be nearly net-shaped via LPBF and exhibit favorable physical properties, including a low elastic modulus, high hydrophilicity, a specific linear expansion rate, as well as

superelastic and shape memory effects. These scaffolds demonstrate excellent biocompatibility, support in vitro osteogenesis, and possess significant in vivo bone ingrowth capabilities. When compared to titanium alloys, NiTi alloys show comparable osteogenic properties in vitro but superior bone ingrowth properties in vivo. Additionally, among octahedral-type, torsion-type, and topologically optimized compression-type porous scaffolds, the latter demonstrates enhanced bone ingrowth properties.

CRediT authorship contribution statement

Jiaming Lin: Writing – original draft, Methodology, Investigation, Formal analysis. **An Yan:** Writing – review & editing, Methodology, Investigation, Formal analysis. **Anfei Huang:** Writing – review & editing, Investigation, Formal analysis. **Qinglian Tang:** Writing – review & editing, Methodology. **Jinchang Lu:** Writing – review & editing, Methodology. **Huaiyuan Xu:** Writing – review & editing, Methodology. **Yufeng Huang:** Writing – review & editing, Investigation. **Tianqi Luo:** Writing – review & editing, Investigation. **Zhihao Chen:** Writing – review & editing, Investigation. **Anyu Zeng:** Writing – review & editing, Investigation. **Xiaojun Zhu:** Writing – review & editing, Supervision, Methodology, Formal analysis. **Chao Yang:** Writing – review & editing, Supervision, Methodology, Funding acquisition. **Jin Wang:** Writing – review & editing, Supervision, Project administration, Methodology, Funding acquisition.

Declaration of competing interest

The authors declare that they have no known competing financial interests or personal relationships that could have appeared to influence the work reported in this paper.

Acknowledgments

This work was supported by the Key-Area Research and Development Program of Guangdong Province (Grant No. 2020B090923001). No relevant financial activities outside the submitted work.

Appendix A. Supplementary data

Supplementary data to this article can be found online at https://doi.org/10.1016/j.mtbio.2024.101344.

Data availability

Data will be made available on request.

References

[1] M. Meng, J. Wang, H. Huang, X. Liu, J. Zhang, Z. Li, 3D printing metal implants in orthopedic surgery: methods, applications and future prospects, J. Orthop. Transl. (2023), https://doi.org/10.1016/j.jot.2023.08.004.
[2] H. Yu, M. Xu, Q. Duan, Y. Li, Y. Liu, L. Song, L. Cheng, J. Ying, D. Zhao, 3D-printed porous tantalum artificial bone scaffolds: fabrication, properties, and applications, Biomed. Mater. 19 (2024), https://doi.org/10.1088/1748-605X/ad46d2.
[3] W. Liang, C. Zhou, H. Zhang, J. Bai, B. Jiang, C. Jiang, W. Ming, H. Zhang, H. Long, X. Huang, J. Zhao, Recent advances in 3D printing of biodegradable metals for orthopaedic applications, J. Biol. Eng. 17 (2023) 1–24, https://doi.org/10.1186/s13036-023-00371-7.
[4] J. Zhao, Y. Zhang, Y. Xia, X. Wang, S. Xu, Y. Xie, Application of an arched, Ni–Ti shape-memory connector in repairing distal tibiofibular syndesmosis ligament injury, BMC Muscoskel. Disord. (2022), https://doi.org/10.1186/s12891-022-05449-9.
[5] Y. Wang, D. Xia, X. Luo, H. Zhang, J. Wu, P. Zhou, S. Xu, Comparison of the kirschner wire tension band with a novel nickel-titanium arched shape-memory alloy connector in transverse patellar fractures: a retrospective study, J. Knee Surg. (2021), https://doi.org/10.1055/s-0039-3402802.
[6] M. Song, Y. Su, C. Li, Y. Xu, Evaluation of the mechanical properties and clinical application of nickel–titanium shape memory alloy scaphoid arc nail, Eng. Life Sci. (2021), https://doi.org/10.1002/elsc.202000055.
[7] P.Y. Zhou, L.Q. Jiang, D.M. Xia, J.H. Wu, Y. Ye, S.G. Xu, Nickel-titanium arched shape-memory alloy connector combined with bone grafting in the treatment of scaphoid nonunion, Eur. J. Med. Res. (2019), https://doi.org/10.1186/s40001-019-0380-y.
[8] Z.C. Hao, Y. Xia, J.H. Wu, Y.T. Zhang, S.G. Xu, Application of a Ni-Ti arched shape-memory connector in unstable lateral malleolus fractures: a retrospective study, Injury (2019), https://doi.org/10.1016/j.injury.2018.10.037.
[9] E. Topolnitskiy, T. Chekalkin, E. Marchenko, Y. Yasenchuk, S.B. Kang, J.H. Kang, A. Obrosov, Evaluation of clinical performance of tini-based implants used in chest wall repair after resection for malignant tumors, J. Funct. Biomater. (2021), https://doi.org/10.3390/jfb12040060.
[10] J. Ryhänen, A. Leminen, T. Jämsä, J. Tuukkanen, A. Pramila, T. Raatikainen, A novel treatment of grade III acromioclavicular joint dislocations with a C-hook implant, Arch. Orthop. Trauma Surg. (2006), https://doi.org/10.1007/s00402-005-0074-5.
[11] Q.M. Zhao, H.L. Yang, L. Wang, Z.T. Liu, X.F. Gu, Treatment of comminuted patellar fracture with the nitinol patellar concentrator, Minim Invasive Ther. Allied Technol. (2016), https://doi.org/10.3109/13645706.2015.1134577.
[12] X. Liu, S. Xu, C. Zhang, J. Su, B. Yu, Application of a shape-memory alloy internal fixator for treatment of acetabular fractures with a follow-up of two to nine years in China, Int. Orthop. (2010), https://doi.org/10.1007/s00264-009-0867-1.
[13] J.P.Y. Cheung, D. Samartzis, K. Yeung, M. To, K.D.K. Luk, K.M.C. Cheung, A randomized double-blinded clinical trial to evaluate the safety and efficacy of a novel superelastic nickel–titanium spinal rod in adolescent idiopathic scoliosis: 5-year follow-up, Eur. Spine J. (2018), https://doi.org/10.1007/s00586-017-5245-x.
[14] F.H. Abduljabbar, A.M. Makhdom, M. Rajeh, A.R. Tales, J. Mathew, J. Ouellet, M. Weber, P. Jarzem, Factors associated with clinical outcomes after lumbar interbody fusion with a porous nitinol implant, Global Spine J. (2017), https://doi.org/10.1177/2192568217696693.
[15] F. Mei, X. Ren, W. Wang, The biomechanical effect and clinical application of a Ni-Ti shape memory expansion clamp, Spine (1997), https://doi.org/10.1097/00007632-199709150-00004.
[16] T. Ji, Y. Yang, X. Tang, H. Liang, T. Yan, R. Yang, W. Guo, 3D-Printed modular hemipelvic endoprosthetic reconstruction following periacetabular tumor resection: early results of 80 consecutive cases, J. Bone Jt. Surg. (2020), https://doi.org/10.2106/JBJS.19.01437.
[17] J. Markhoff, J. Wieding, V. Weissmann, J. Pasold, A. Jonitz-Heincke, R. Bader, Influence of different three-dimensional open porous titanium scaffold designs on human osteoblasts behavior in static and dynamic cell investigations, Materials (2015), https://doi.org/10.3390/ma8085259.
[18] S. Van Bael, Y.C. Chai, S. Truscello, M. Moesen, G. Kerckhofs, H. Van Oosterwyck, J.P. Kruth, J. Schrooten, The effect of pore geometry on the in vitro biological behavior of human periosteum-derived cells seeded on selective laser-melted Ti6Al4V bone scaffolds, Acta Biomater. (2012), https://doi.org/10.1016/j.actbio.2012.04.001.
[19] Y.T. Jian, Y. Yang, T. Tian, C. Stanford, X.P. Zhang, K. Zhao, Effect of pore size and porosity on the biomechanical properties and cytocompatibility of porous NiTi alloys, PLoS One (2015), https://doi.org/10.1371/journal.pone.0128138.
[20] I. Gotman, D. Ben-David, R.E. Unger, T. Böse, E.Y. Gutmanas, C.J. Kirkpatrick, Mesenchymal stem cell proliferation and differentiation on load-bearing trabecular Nitinol scaffolds, Acta Biomater. (2013), https://doi.org/10.1016/j.actbio.2013.05.030.
[21] J. Li, H. Yang, H. Wang, J. Ruan, Low elastic modulus titanium-nickel scaffolds for bone implants, Mater. Sci. Eng. C (2014), https://doi.org/10.1016/j.msec.2013.08.043.
[22] H. Aihara, J. Zider, G. Fanton, T. Duerig, Combustion synthesis porous nitinol for biomedical applications, Int. J. Biomater. (2019), https://doi.org/10.1155/2019/4307461.
[23] S.J. Simske, R. Sachdeva, Cranial bone apposition and ingrowth in a porous nickel–titanium implant, J. Biomed. Mater. Res. (1995), https://doi.org/10.1002/jbm.820290413.
[24] F. Likibi, G. Chabot, M. Assad, C.H. Rivard, Influence of orthopedic implant structure on adjacent bone density and on stability, Am. J. Orthoped. (2008).
[25] H. Naujokat, A.I. Gökkaya, Y. Açil, K. Loger, T. Klüter, S. Fuchs, J. Wiltfang, In vivo biocompatibility evaluation of 3D-printed nickel–titanium fabricated by selective laser melting, J. Mater. Sci. Mater. Med. (2022), https://doi.org/10.1007/s10856-022-06641-y.
[26] H.Z. Lu, H.W. Ma, X. Luo, Y. Wang, J. Wang, R. Lupoi, S. Yin, C. Yang, Microstructure, shape memory properties, and in vitro biocompatibility of porous NiTi scaffolds fabricated via selective laser melting, J. Mater. Res. Technol. (2021), https://doi.org/10.1016/j.jmrt.2021.11.112.
[27] T. Habijan, C. Haberland, H. Meier, J. Frenzel, J. Wittsiepe, C. Wuwer, C. Greulich, T.A. Schildhauer, M. Köller, The biocompatibility of dense and porous Nickel-Titanium produced by selective laser melting, Mater. Sci. Eng. C (2013), https://doi.org/10.1016/j.msec.2012.09.008.
[28] W. Hoffmann, T. Bormann, A. Rossi, B. Müller, R. Schumacher, I. Martin, M. de Wild, D. Wendt, Rapid prototyped porous nickel–titanium scaffolds as bone substitutes, J. Tissue Eng. (2014), https://doi.org/10.1177/2041731414540674.
[29] S. Strauß, S. Dudziak, R. Hagemann, S. Barcikowski, M. Fliess, M. Israelowitz, D. Kracht, J.W. Kuhbier, C. Radtke, K. Reimers, P.M. Vogt, Induction of osteogenic differentiation of adipose derived stem cells by microstructured nitinol actuator-mediated mechanical stress, PLoS One (2012), https://doi.org/10.1371/journal.pone.0051264.
[30] Y.J. Liu, D.C. Ren, S.J. Li, H. Wang, L.C. Zhang, T.B. Sercombe, Enhanced fatigue characteristics of a topology-optimized porous titanium structure produced by

selective laser melting, Addit. Manuf. (2020), https://doi.org/10.1016/j.addma.2020.101060.
[31] P. Liu, Z. Kang, Y. Luo, Two-scale concurrent topology optimization of lattice structures with connectable microstructures, Addit. Manuf. (2020), https://doi.org/10.1016/j.addma.2020.101427.
[32] C. Wu, J. Luo, J. Zhong, Y. Xu, B. Wan, W. Huang, J. Fang, G.P. Steven, G. Sun, Q. Li, Topology optimisation for design and additive manufacturing of functionally graded lattice structures using derivative-aware machine learning algorithms, Addit. Manuf. (2023), https://doi.org/10.1016/j.addma.2023.103833.
[33] L. Zhao, L. Liu, Z. Wu, Y. Zhang, P.K. Chu, Effects of micropitted/nanotubular titania topographies on bone mesenchymal stem cell osteogenic differentiation, Biomaterials (2012), https://doi.org/10.1016/j.biomaterials.2011.12.024.
[34] F. Rupp, L. Scheideier, N. Olshanska, M. De Wild, M. Wieland, J. Geis-Gerstorfer, Enhancing surface free energy and hydrophilicity through chemical modification of microstructured titanium implant surfaces, J. Biomed. Mater. Res. Part A - Part A (2006), https://doi.org/10.1002/jbm.a.30518.
[35] C.R. Bragdon, M. Jasty, M. Greene, H.E. Rubash, W.H. Harris, Biologic fixation of total hip implants: insights gained from a series of canine studies, J. Bone Jt. Surg. (2004), https://doi.org/10.2106/00004623-200412002-00015.
[36] V. Karageorgiou, D. Kaplan, Porosity of 3D biomaterial scaffolds and osteogenesis, Biomaterials (2005), https://doi.org/10.1016/j.biomaterials.2005.02.002.
[37] C.M. Murphy, M.G. Haugh, F.J. O'Brien, The effect of mean pore size on cell attachment, proliferation and migration in collagen-glycosaminoglycan scaffolds for bone tissue engineering, Biomaterials (2010), https://doi.org/10.1016/j.biomaterials.2009.09.063.
[38] M. De Wild, R. Schumacher, K. Mayer, E. Schkommodau, D. Thoma, M. Bredell, A. Kruse Gujer, K.W. Grätz, F.E. Weber, Bone regeneration by the osteoconductivity of porous titanium implants manufactured by selective laser melting: a histological and micro computed tomography study in the rabbit, Tissue Eng. - Part A (2013), https://doi.org/10.1089/ten.tea.2012.0753.
[39] M. De Wild, S. Zimmermann, J. Rüegg, R. Schumacher, T. Fleischmann, C. Ghayor, F.E. Weber, Influence of microarchitecture on osteoconduction and mechanics of porous titanium scaffolds generated by selective laser melting, 3D Print. Addit. Manuf. (2016), https://doi.org/10.1089/3dp.2016.0004.
[40] H.H. Cheng, H.W. Ma, L. ling Pan, X. Luo, L. hua Liu, H.K. Dong, T. Song, F. Wang, C. Yang, Manufacturability and mechanical properties of Ti-35Nb-7Zr-5Ta porous titanium alloys produced by laser powder-bed fusion, Addit. Manuf. 86 (2024), https://doi.org/10.1016/j.addma.2024.104190.
[41] A. Yan, W.S. Cai, H.Z. Li, H.Z. Lu, J.M. Lin, J. Wang, L.C. Zhang, C. Yang, Stable superelasticity with large recoverable strain in NiTi alloy via additive manufacturing, Mater. Sci. Eng. A. 911 (2024), https://doi.org/10.1016/j.msea.2024.146935.
[42] M. Es-Souni, M. Es-Souni, H. Fischer-Brandies, Assessing the biocompatibility of NiTi shape memory alloys used for medical applications, Anal. Bioanal. Chem. (2005), https://doi.org/10.1007/s00216-004-2888-3.
[43] D.J. Wever, A.G. Veldhuizen, J. De Vries, H.J. Busscher, D.R.A. Uges, J.R. Van Horn, Electrochemical and surface characterization of a nickel-titanium alloy, Biomaterials (1998), https://doi.org/10.1016/S0142-9612(97)00210-X.
[44] O. Cissé, O. Savadogo, M. Wu, L.H. Yahia, Effect of surface treatment of NiTi alloy on its corrosion behavior in Hanks' solution, J. Biomed. Mater. Res. (2002), https://doi.org/10.1002/jbm.10114.
[45] B. O'Brien, W.M. Carroll, M.J. Kelly, Passivation of nitinol wire for vascular implants - a demonstration of the benefits, Biomaterials (2002), https://doi.org/10.1016/S0142-9612(01)00299-X.
[46] T. Habijan, O. Bremm, S.A. Esenwein, G. Muhr, M. Koller, Influence of nickel ions on human multipotent mesenchymal stromal cells (hMSCs), Mater. Werkst. (2007), https://doi.org/10.1002/mawe.200700231.
[47] M. Taira, M.S. Toguchi, Y. Hamada, M. Okazaki, J. Takahashi, R. Ito, S. Toyosawa, N. Ijyuin, Studies on cytotoxicity of nickel ions using C3H10T1/2 fibroblast cells, J. Oral Rehabil. (2000), https://doi.org/10.1111/j.1365-2842.2000.00608.x.
[48] European Parliament and Council Directive, 94/27/EC of 30 June 1994 amending for the 12th time Directive 76/769/EEC on the approximation of the laws, regulations and administrative provisions of the Member States relating to restrictions on the marketing a, off, J. Eur. Communities. L181 (1994) 1–2.
[49] FDA UCM296980. http://www.fda.gov/downloads/MedicalDevices/NewsEvents/WorkshopsConferences/UCM296980.pdf., (n.d.).
[50] F.W. Sunderman, Potential toxicity from nickel contamination of intravenous fluids, Ann. Clin. Lab. Sci. (1983).
[51] W. Hoffmann, T. Bormann, A. Kessler, D. Wendt, M. De Wild, Ni release from rapid prototyped 3D NiTi scaffolds, Eur. Cell. Mater. 28 (2014) 2262.
[52] T. Habijan, T. Glogowski, S. Kühn, M. Pohl, J. Wittsiepe, C. Greulich, G. Eggeler, T. A. Schildhauer, M. Köller, Can human mesenchymal stem cells survive on a NiTi implant material subjected to cyclic loading? Acta Biomater. (2011) https://doi.org/10.1016/j.actbio.2011.02.022.
[53] K.W. Widantha, E.A. Basuki, E. Martides, B. Prawara, Effect of hydroxyapatite/alumina composite coatings using HVOF on immersion behavior of NiTi alloys, J. Biomater. Appl. (2021), https://doi.org/10.1177/08853282211022531.
[54] R. Ion, C. Luculescu, A. Cimpean, P. Marx, D.M. Gordin, T. Gloriant, Nitride coating enhances endothelialization on biomedical NiTi shape memory alloy, Mater. Sci. Eng. C (2016), https://doi.org/10.1016/j.msec.2016.02.031.
[55] S. Wu, X. Liu, Y.L. Chan, P.K. Chu, C.Y. Chung, C. Chu, K.W.K. Yeung, W.W. Lu, K. M.C. Cheung, K.D.K. Luk, Nickel release behavior and surface characteristics of porous NiTi shape memory alloy modified by different chemical processes, J. Biomed. Mater. Res., Part A (2009), https://doi.org/10.1002/jbm.a.32008.
[56] J. Choi, D. Bogdanski, M. Köller, S.A. Esenwein, D. Müller, G. Muhr, M. Epple, Calcium phosphate coating of nickel-titanium shape-memory alloys, Coating procedure and adherence of leukocytes and platelets, Biomaterials (2003), https://doi.org/10.1016/S0142-9612(03)00241-2.
[57] Y. Zhang, S. Attarilar, L. Wang, W. Lu, J. Yang, Y. Fu, A review on design and mechanical properties of additively manufactured NiTi implants for orthopedic applications, Int. J. Bioprinting. (2021), https://doi.org/10.18063/IJB.V7I2.340.
[58] S. Das, Physical aspects of process control in selective laser sintering of metals, Adv. Eng. Mater. (2003), https://doi.org/10.1002/adem.200310099.
[59] J. Sam, B. Franco, J. Ma, I. Karaman, A. Elwany, J.H. Mabe, Tensile actuation response of additively manufactured nickel-titanium shape memory alloys, Scripta Mater. (2018), https://doi.org/10.1016/j.scriptamat.2017.11.013.
[60] K. Kapat, P.K. Srivas, A.P. Rameshbabu, P.P. Maity, S. Jana, J. Dutta, P. Majumdar, D. Chakrabarti, S. Dhara, Influence of porosity and pore-size distribution in Ti6Al4v foam on physicomechanical properties, osteogenesis, and quantitative validation of bone ingrowth by micro-computed tomography, ACS Appl. Mater. Interfaces (2017), https://doi.org/10.1021/acsami.7b13960.
[61] Y. Sun, Z. Zhang, Q. Liu, L. Ren, J. Wang, In vitro evaluation of the biocompatibility and bioactivity of a SLM-fabricated NiTi alloy with superior tensile property, J. Mater. Sci. Mater. Med. 35 (2024), https://doi.org/10.1007/s10856-024-06822-x.
[62] M. N W N A, A. R, K.A. N H, S. E, K. M A A, I. M H, T. L K, S. M Z, In vitro evaluation of cytotoxicity and genotoxicity of porous nickel titanium dental implants produced by metal injection molding technique, J. Biomed. Mater. Res. B Appl. Biomater. (2024), https://doi.org/10.1002/jbm.b.35306.
[63] N.W.N.A. Mustafa, R. Ahmad, M.A. Ahmad Khushaini, N.H. Kamar Affendi, S. M. Ab Ghani, S.K. Tan, M.H. Ismail, C.L. Goo, M.Z. Kassim, T.W. Lim, L.K. Teh, Porous NiTi dental implant fabricated by a metal injection molding: an in vivo biocompatibility evaluation in an animal model, ACS Biomater. Sci. Eng. (2024), https://doi.org/10.1021/acsbiomaterials.3c01551.
[64] M. Assad, A. Chernyshov, M.A. Leroux, C.H. Rivard, A new porous titanium-nickel alloy: Part 2. Sensitization, irritation and acute systemic toxicity evaluation, Bio Med. Mater. Eng. (2002).
[65] M. Assad, A. Chernyshov, M.A. Leroux, C.H. Rivard, A new porous titanium-nickel alloy: Part 1. Cytotoxicity and genotoxicity evaluation, Bio Med. Mater. Eng. (2002).
[66] O.V. Kokorev, V.N. Hodorenko, T.L. Chekalkin, J.S. Kim, S.B. Kang, G.T. Dambaev, V.E. Gunther, In vitro and in vivo evaluation of porous TiNi-based alloy as a scaffold for cell tissue engineering, Artif. Cells, Nanomedicine Biotechnol (2016), https://doi.org/10.3109/21691401.2014.982799.
[67] O. Prymak, D. Bogdanski, M. Köller, S.A. Esenwein, G. Muhr, F. Beckmann, T. Donath, M. Assad, M. Epple, Morphological characterization and in vitro biocompatibility of a porous nickel-titanium alloy, Biomaterials (2005), https://doi.org/10.1016/j.biomaterials.2005.02.029.
[68] M. Zhang, R. Lin, X. Wang, J. Xue, C. Deng, C. Feng, H. Zhuang, J. Ma, C. Qin, L. Wan, J. Chang, C. Wu, 3D printing of Haversian bone-mimicking scaffolds for multicellular delivery in bone regeneration, Sci. Adv. (2020), https://doi.org/10.1126/sciadv.aaz6725.
[69] Y. Zuo, X. Liu, D. Wei, J. Sun, W. Xiao, H. Zhao, L. Guo, Q. Wei, H. Fan, X. Zhang, Photo-cross-linkable methacrylated gelatin and hydroxyapatite hybrid hydrogel for modularly engineering biomimetic osteon, ACS Appl. Mater. Interfaces (2015), https://doi.org/10.1021/acsami.5b01433.
[70] M.R. Dias, P.R. Fernandes, J.M. Guedes, S.J. Hollister, Permeability analysis of scaffolds for bone tissue engineering, J. Biomech. (2012), https://doi.org/10.1016/j.jbiomech.2012.01.019.
[71] T.S. Karande, J.L. Ong, C.M. Agrawal, Diffusion in musculoskeletal tissue engineering scaffolds: design issues related to porosity, permeability, architecture, and nutrient mixing, Ann. Biomed. Eng. (2004), https://doi.org/10.1007/s10439-004-7825-2.
[72] E.A. Botchwey, M.A. Dupree, S.R. Pollack, E.M. Levine, C.T. Laurencin, Tissue engineered bone: measurement of nutrient transport in three-dimensional matrices, J. Biomed. Mater. Res., Part A (2003), https://doi.org/10.1002/jbm.a.10111.
[73] S. Impens, Y. Chen, S. Mullens, F. Luyten, J. Schrooten, Controlled cell-seeding methodologies: a first step toward clinically relevant bone tissue engineering strategies, Tissue Eng. C Methods (2010), https://doi.org/10.1089/ten.tec.2010.0069.
[74] Z. P, Y. Q, M. F, L. N, X. Y, W. B, W. L, Adhesion, proliferation and osteogenic differentiation of mesenchymal stem cells in 3D printed poly-ε-caprolactone/hydroxyapatite scaffolds combined with bone marrow clots, Mol. Med. Rep. (2017).
[75] X. Wei, D. Zhao, B. Wang, W. Wang, K. Kang, H. Xie, B. Liu, X. Zhang, J. Zhang, Z. Yang, Tantalum coating of porous carbon scaffold supplemented with autologous bone marrow stromal stem cells for bone regeneration in vitro and in vivo, Exp. Biol. Med. (2016), https://doi.org/10.1177/1535370216629578.
[76] F.P.W. Melchels, A.M.C. Barradas, C.A. Van Blitterswijk, J. De Boer, J. Feijen, D. W. Grijpma, Effects of the architecture of tissue engineering scaffolds on cell seeding and culturing, Acta Biomater. (2010), https://doi.org/10.1016/j.actbio.2010.06.012.
[77] G. Li, L. Wang, W. Pan, F. Yang, W. Jiang, X. Wu, X. Kong, K. Dai, Y. Hao, In vitro and in vivo study of additive manufactured porous Ti6Al4V scaffolds for repairing bone defects, Sci. Rep. (2016), https://doi.org/10.1038/srep34072.
[78] A.G. Mitsak, J.M. Kemppainen, M.T. Harris, S.J. Hollister, Effect of polycaprolactone scaffold permeability on bone regeneration in vivo, Tissue Eng. - Part A. https://doi.org/10.1089/ten.tea.2010.0560, 2011.
[79] C.M. Agrawal, J.S. McKinney, D. Lanctot, K.A. Athanasiou, Effects of fluid flow on the in vitro degradation kinetics of biodegradable scaffolds for tissue engineering, Biomaterials (2000), https://doi.org/10.1016/S0142-9612(00)00112-5.

[80] T. Mygind, M. Stiehler, A. Baatrup, H. Li, X. Zou, A. Flyvbjerg, M. Kassem, C. Bünger, Mesenchymal stem cell ingrowth and differentiation on coralline hydroxyapatite scaffolds, Biomaterials (2007), https://doi.org/10.1016/j.biomaterials.2006.10.003.

[81] O.V. Kokorev, V.N. Khodorenko, A.A. Radkevich, G.T. Dambaev, V.E. Gunter, Development and differentiation of mesenchymal bone marrow cells in porous permeable titanium nickelide implants in vitro and in vivo, Bull. Exp. Biol. Med. (2016), https://doi.org/10.1007/s10517-016-3465-4.

[82] S. Kujala, J. Ryhänen, A. Danilov, J. Tuukkanen, Effect of porosity on the osteointegration and bone ingrowth of a weight-bearing nickel-titanium bone graft substitute, Biomaterials (2003), https://doi.org/10.1016/S0142-9612(03)00359-4.

[83] S.B. Kang, K.S. Yoon, J.S. Kim, T.H. Nam, V.E. Gjunter, In vivo result of porous TiNi shape memory alloy: bone response and growth, Mater. Trans. (2002), https://doi.org/10.2320/matertrans.43.1045.